EIGHT ULTRA-FAINT GALAXY CANDIDATES DISCOVERED IN YEAR TWO OF THE DARK ENERGY SURVEY

A. DRLICA-WAGNER[1], K. BECHTOL[2,3], E. S. RYKOFF[4,5], E. LUQUE[6,7], A. QUEIROZ[6,7], Y.-Y. MAO[4,5,8], R. H. WECHSLER[4,5,8], J. D. SIMON[9], B. SANTIAGO[6,7], B. YANNY[1], E. BALBINOT[7,10], S. DODELSON[1,11], A. FAUSTI NETO[7], D. J. JAMES[12], T. S. LI[13], M. A. G. MAIA[7,14], J. L. MARSHALL[13], A. PIERES[6,7], K. STRINGER[13], A. R. WALKER[12], T. M. C. ABBOTT[12], F. B. ABDALLA[15,16], S. ALLAM[1], A. BENOIT-LÉVY[15], G. M. BERNSTEIN[17], E. BERTIN[18,19], D. BROOKS[15], E. BUCKLEY-GEER[1], D. L. BURKE[4,5], A. CARNERO ROSELL[7,14], M. CARRASCO KIND[20,21], J. CARRETERO[22,23], M. CROCCE[22], L. N. DA COSTA[7,14], S. DESAI[24,25], H. T. DIEHL[1], J. P. DIETRICH[24,25], P. DOEL[15], T. F. EIFLER[17,26], A. E. EVRARD[27,28], D. A. FINLEY[1], B. FLAUGHER[1], P. FOSALBA[22], J. FRIEMAN[1,11], E. GAZTANAGA[22], D. W. GERDES[28], D. GRUEN[29,30], R. A. GRUENDL[20,21], G. GUTIERREZ[1], K. HONSCHEID[31,32], K. KUEHN[33], N. KUROPATKIN[1], O. LAHAV[15], P. MARTINI[31,34], R. MIQUEL[23,35], B. NORD[1], R. OGANDO[7,14], A. A. PLAZAS[26], K. REIL[5], A. ROODMAN[4,5], M. SAKO[17], E. SANCHEZ[36], V. SCARPINE[1], M. SCHUBNELL[28], I. SEVILLA-NOARBE[20,36], R. C. SMITH[12], M. SOARES-SANTOS[1], F. SOBREIRA[1,7], E. SUCHYTA[31,32], M. E. C. SWANSON[21], G. TARLE[28], D. TUCKER[1], V. VIKRAM[37], W. WESTER[1], Y. ZHANG[28], AND J. ZUNTZ[38]

(THE DES COLLABORATION)

[1] Fermi National Accelerator Laboratory, P.O. Box 500, Batavia, IL 60510, USA; kadrlica@fnal.gov
[2] Wisconsin IceCube Particle Astrophysics Center (WIPAC), Madison, WI 53703, USA; keith.bechtol@icecube.wisc.edu
[3] Department of Physics, University of Wisconsin–Madison, Madison, WI 53706, USA
[4] Kavli Institute for Particle Astrophysics & Cosmology, P.O. Box 2450, Stanford University, Stanford, CA 94305, USA
[5] SLAC National Accelerator Laboratory, Menlo Park, CA 94025, USA
[6] Instituto de Física, UFRGS, Caixa Postal 15051, Porto Alegre, RS-91501-970, Brazil
[7] Laboratório Interinstitucional de e-Astronomia—LIneA, Rua Gal. José Cristino 77, Rio de Janeiro, RJ-20921-400, Brazil
[8] Department of Physics, Stanford University, 382 Via Pueblo Mall, Stanford, CA 94305, USA
[9] Carnegie Observatories, 813 Santa Barbara St., Pasadena, CA 91101, USA
[10] Department of Physics, University of Surrey, Guildford GU2 7XH, UK
[11] Kavli Institute for Cosmological Physics, University of Chicago, Chicago, IL 60637, USA
[12] Cerro Tololo Inter-American Observatory, National Optical Astronomy Observatory, Casilla 603, La Serena, Chile
[13] George P. and Cynthia Woods Mitchell Institute for Fundamental Physics and Astronomy, and Department of Physics and Astronomy, Texas A&M University, College Station, TX 77843, USA
[14] Observatório Nacional, Rua Gal. José Cristino 77, Rio de Janeiro, RJ-20921-400, Brazil
[15] Department of Physics & Astronomy, University College London, Gower Street, London, WC1E 6BT, UK
[16] Department of Physics and Electronics, Rhodes University, P.O. Box 94, Grahamstown, 6140, South Africa
[17] Department of Physics and Astronomy, University of Pennsylvania, Philadelphia, PA 19104, USA
[18] CNRS, UMR 7095, Institut d'Astrophysique de Paris, F-75014, Paris, France
[19] Sorbonne Universités, UPMC Univ Paris 06, UMR 7095, Institut d'Astrophysique de Paris, F-75014, Paris, France
[20] Department of Astronomy, University of Illinois, 1002 W. Green Street, Urbana, IL 61801, USA
[21] National Center for Supercomputing Applications, 1205 West Clark St., Urbana, IL 61801, USA
[22] Institut de Ciències de l'Espai, IEEC-CSIC, Campus UAB, Carrer de Can Magrans, s/n, E-08193 Bellaterra, Barcelona, Spain
[23] Institut de Física d'Altes Energies, Universitat Autònoma de Barcelona, E-08193 Bellaterra, Barcelona, Spain
[24] Excellence Cluster Universe, Boltzmannstr. 2, D-85748 Garching, Germany
[25] Faculty of Physics, Ludwig-Maximilians University, Scheinerstr. 1, D-81679 Munich, Germany
[26] Jet Propulsion Laboratory, California Institute of Technology, 4800 Oak Grove Dr., Pasadena, CA 91109, USA
[27] Department of Astronomy, University of Michigan, Ann Arbor, MI 48109, USA
[28] Department of Physics, University of Michigan, Ann Arbor, MI 48109, USA
[29] Max Planck Institute for Extraterrestrial Physics, Giessenbachstrasse, D-85748 Garching, Germany
[30] Universitäts-Sternwarte, Fakultät für Physik, Ludwig-Maximilians Universität München, Scheinerstr. 1, D-81679 München, Germany
[31] Center for Cosmology and Astro-Particle Physics, The Ohio State University, Columbus, OH 43210, USA
[32] Department of Physics, The Ohio State University, Columbus, OH 43210, USA
[33] Australian Astronomical Observatory, North Ryde, NSW 2113, Australia
[34] Department of Astronomy, The Ohio State University, Columbus, OH 43210, USA
[35] Institució Catalana de Recerca i Estudis Avançats, E-08010 Barcelona, Spain
[36] Centro de Investigaciones Energéticas, Medioambientales y Tecnológicas (CIEMAT), Madrid, Spain
[37] Argonne National Laboratory, 9700 South Cass Avenue, Lemont, IL 60439, USA
[38] Jodrell Bank Center for Astrophysics, School of Physics and Astronomy, University of Manchester, Oxford Road, Manchester, M13 9PL, UK

ABSTRACT

We report the discovery of eight new ultra-faint dwarf galaxy candidates in the second year of optical imaging data from the Dark Energy Survey (DES). Six of these candidates are detected at high confidence, while two lower-confidence candidates are identified in regions of non-uniform survey coverage. The new stellar systems are found by three independent automated search techniques and are identified as overdensities of stars, consistent with the isochrone and luminosity function of an old and metal-poor simple stellar population. The new systems are faint ($M_V > -4.7$ mag) and span a range of physical sizes (17 pc $< r_{1/2} < 181$ pc) and heliocentric distances (25 kpc $< D_\odot < 214$ kpc). All of the new systems have central surface brightnesses consistent with known ultra-faint dwarf galaxies ($\mu \gtrsim 27.5$ mag arcsec^{-2}). Roughly half of the DES candidates are more distant, less luminous, and/or have lower surface brightnesses than previously known Milky Way satellite galaxies. Most of the

1

candidates are found in the southern part of the DES footprint close to the Magellanic Clouds. We find that the DES data alone exclude ($p < 10^{-3}$) a spatially isotropic distribution of Milky Way satellites and that the observed distribution can be well, though not uniquely, described by an association between several of the DES satellites and the Magellanic system. Our model predicts that the full sky may hold $\sim$100 ultra-faint galaxies with physical properties comparable to the DES satellites and that 20%–30% of these would be spatially associated with the Magellanic Clouds.

Key words: galaxies: dwarf – Local Group

1. INTRODUCTION

The population of Milky Way satellite galaxies includes the least luminous, least chemically enriched, and most dark matter dominated galaxies in the known universe (e.g., Simon & Geha 2007; Kirby et al. 2008). Although they are extreme systems from an observational perspective, low-luminosity dwarf spheroidal galaxies are likely to be the most common galaxy type by number. This duality places the emerging population of near-field galaxies in a unique position to allow the testing of models of galaxy formation and the cold dark matter paradigm (e.g., Bullock et al. 2001), and has motivated studies ranging from the physical conditions at the time of reionization (e.g., Bullock et al. 2000; Benson et al. 2002), to the particle properties of dark matter (e.g., Ackermann et al. 2015; Geringer-Sameth et al. 2015a).

Milky Way satellite galaxies are typically discovered as arcminute-scale statistical overdensities of individually resolved stars in wide-field optical imaging surveys (Willman 2010, and the references therein). Prior to 2005, there were 12 known "classical" Milky Way satellite galaxies with absolute magnitudes in the range $-8\,\mathrm{mag} \gtrsim M_V \gtrsim -18\,\mathrm{mag}$ (McConnachie 2012). From 2005 to 2014, 15 ultra-faint satellite galaxies with $M_V \gtrsim -8\,\mathrm{mag}$ were identified in Sloan Digital Sky Survey (SDSS; York et al. 2000) data through a combination of systematic searches (Willman et al. 2005a, 2005b; Belokurov et al. 2006, 2007, 2008, 2009, 2010; Grillmair 2006, 2009; Sakamoto & Hasegawa 2006; Zucker et al. 2006a, 2006b; Irwin et al. 2007; Walsh et al. 2007) and dedicated spectroscopic follow-up observations (Kleyna et al. 2005; Muñoz et al. 2006; Martin et al. 2007; Simon & Geha 2007; Adén et al. 2009; Belokurov et al. 2009; Carlin et al. 2009; Geha et al. 2009; Koch et al. 2009; Walker et al. 2009; Koposov et al. 2011; Simon et al. 2011; Willman et al. 2011; Kirby et al. 2013). Several outer halo star clusters and/or more compact stellar systems of uncertain classification were reported during roughly the same period (e.g., Koposov et al. 2007; Walsh et al. 2009; Belokurov et al. 2010, 2014; Muñoz et al. 2012; Balbinot et al. 2013; Laevens et al. 2014; Kim & Jerjen 2015a; Kim et al. 2015b). Dwarf galaxies are distinguished from star clusters by having a dynamical mass that is substantially larger than the mass inferred from the luminous stellar population and/or a significant dispersion in stellar metallicities indicative of multiple generations of star formation and a gravitational potential deep enough to retain supernova ejecta (Willman & Strader 2012).

Since the beginning of 2015, a combination of new optical imaging surveys and a reanalysis of SDSS data have resulted in the detection of 14 additional Milky Way companions, tentatively classified as dwarf galaxies (Bechtol et al. 2015; Kim & Jerjen 2015b; Kim et al. 2015a; Koposov et al. 2015a; Laevens et al. 2015a, 2015b; Martin et al. 2015). The new galaxy candidates have been examined for their (lack of) neutral gas (Westmeier et al. 2015), possible association with the

Magellanic Clouds (Deason et al. 2015; Yozin & Bekki 2015), and spatial distribution within the Galactic halo (Pawlowski et al. 2015), and have become targets for indirect dark matter searches (Drlica-Wagner et al. 2015; Geringer-Sameth et al. 2015b; Hooper & Linden 2015). The provisional classification of these stellar systems as dwarf galaxies relies on their low surface brightnesses, large physical sizes, large ellipticities, and/or large heliocentric distances. However, some of these objects lie in a region of size–luminosity space where the distinction between dwarf galaxy and globular cluster is ambiguous. Thus far, spectroscopic observations have confirmed that three of the recently discovered satellites, Reticulum II (Koposov et al. 2015b; Simon et al. 2015; Walker et al. 2015), Horologium I (Koposov et al. 2015b), and Hydra II (Kirby et al. 2015) possess the kinematic and chemical signatures of galaxies.

The Dark Energy Survey (DES; Abbott et al. 2005), which began science operations in late 2013, has already had a large impact on our census of Milky Way substructures. In the first year of DES data, nine new dwarf galaxy candidates were discovered in a region spanning less than 10% of the southern hemisphere (Bechtol et al. 2015; Kim & Jerjen 2015b; Koposov et al. 2015a).[39] Here, we present an extension of the analysis described in Bechtol et al. (2015), incorporating the second year of DES observations to expand the survey coverage from $\sim$1800 deg^2 to $\sim$5000 deg^2 (Figure 1). In Section 2, we discuss the data reduction and catalog generation steps applied to the two-year DES data set and the resulting unique catalog of calibrated objects. We review the various algorithms applied to the DES data to search for ultra-faint galaxies in Section 3 and describe our candidate selection criteria in Section 4. The eight most significant stellar overdensities that are unassociated with previously known systems are reported in Section 5. If these objects are confirmed to be ultra-faint dwarf galaxies, they will be named after their resident constellations—Cetus II (DES J0117–1725), Columba I (DES J0531–2801), Grus II (DES J2204–4626), Indus II (DES J2038–4609).[40] Reticulum III (DES J0345–6026), Tucana III (DES J2356–5935), Tucana IV (DES J0002–6051), and Tucana V (DES J2337–6316)—and named DES 2 through *N* if found to be globular clusters (e.g., Luque et al. 2015). We place the DES candidates in context with other known Local Group galaxies and the Magellanic system in Section 6, and we conclude in Section 7.

---

[39] The system Kim 2/DES J2108.8–5109/Indus I was discovered independently in a separate data set by Kim et al. (2015b) slightly before the DES announcement. With deeper observations, Kim et al concluded that this object is likely a star cluster, and we do not include it in our count of dwarf galaxy candidates.

[40] To distinguish DES J2038–4609 from Kim 2/DES J2108.8–5109/Indus I, we suggest that the new system be designated Indus II if determined to be a dwarf galaxy.
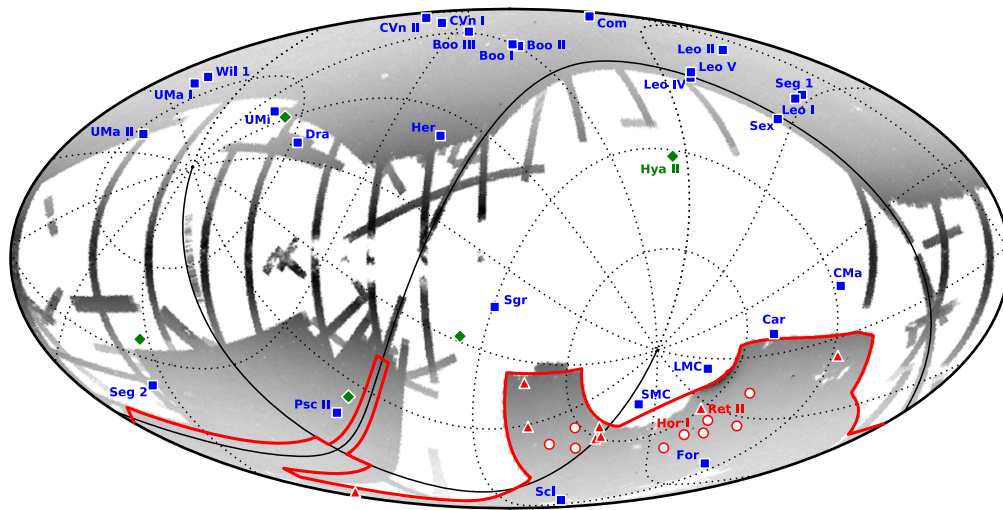
Figure 1. Locations of the eight new dwarf galaxy candidates reported here (red triangles) along with 9 previously reported dwarf galaxy candidates in the DES footprint (red circles; Bechtol et al. 2015; Kim & Jerjen 2015b; Koposov et al. 2015a), 5 recently discovered dwarf galaxy candidates located outside the DES footprint (green diamonds; Kim et al. 2015a; Laevens et al. 2015a, 2015b; Martin et al. 2015), and 27 Milky Way satellite galaxies known prior to 2015 (blue squares; McConnachie 2012). Systems that have been confirmed as satellite galaxies are individually labeled. The figure is shown in Galactic coordinates (Mollweide projection) with the coordinate grid marking the equatorial coordinate system (solid lines for the equator and zero meridian). The grayscale indicates the logarithmic density of stars with $r < 22$ from SDSS and DES. The two-year coverage of DES is ~ 5000 deg^2 and nearly fills the planned DES footprint (outlined in red). For comparison, the Pan-STARRS 1 3π survey covers the region of sky with $\delta_{2000} > -30°$ (Laevens et al. 2015a).

2. DATA SET

DES is an ongoing optical imaging survey of ~ 5000 deg^2 in the south Galactic cap using the Dark Energy Camera (DECam; Flaugher et al. 2015) on the 4-m Blanco Telescope at Cerro Tololo Inter-American Observatory (CTIO). The DECam focal plane comprises 62 2k × 4k CCDs dedicated to science imaging and 12 2k × 2k CCDs for guiding, focus, and alignment. The DECam field of view covers 3 deg^2 with a central pixel scale of 0″.263. DES is scheduled for 525 nights distributed over five years, during which period each point in the survey footprint will be imaged ten times in each of the *grizY* bands (Abbott et al. 2005).

The searches presented in Bechtol et al. (2015) and Luque et al. (2015) utilized an object catalog generated from the coadded images in the DES year-one annual release (Y1A1). To expedite the search for Milky Way satellites in year two, the present analysis uses data products derived from single-epoch imaging instead. This data set is referred to as the DES year-two quick release (Y2Q1), and its construction is summarized below.

2.1. DES Year-two Quick Release

Observations: The Y2Q1 data set consists of 26,590 DECam exposures taken during the first two years of DES observing that pass DES survey quality cuts. Slightly less than half of the DES survey area was observed during the first season (Y1; 2013 August 15–2014 February 9), with typically two to four overlapping exposures, referred to as "tilings," in each of the *grizY* filters. The second season (Y2; 2014 August 7–2015 February 15) covered much of the remaining survey area to a similar depth. Exposures taken in the *griz* bands are 90 s, while *Y*-band exposures are 45 s.

Image Reduction: The DES exposures were processed with the DES data management (DESDM) image detrending pipeline (Sevilla et al. 2011; Desai et al. 2012; Mohr et al. 2012; R.A. Gruendl et al. 2015, in preparation). This pipeline

corrects for cross-talk between CCD amplifier electronics, bias level variations, and pixel-to-pixel sensitivity variations (flat-fielding). Additional corrections are made for nonlinearity, fringing, pupil, and illumination. Both the Y1 and Y2 exposures were reduced with the same image detrending pipeline used to process Y1A1.

Single-epoch Catalog Generation: Astronomical source detection and photometry were performed on a per exposure basis using the `PSFex` and `SExtractor` routines (Bertin & Arnouts 1996; Bertin 2011) in an iterative process (Mohr et al. 2012; R.A. Gruendl et al. 2015, in preparation). As part of this step, astrometric calibration was performed with `SCAMP` (Bertin 2006) by matching objects to the UCAC-4 catalog (Zacharias et al. 2013). The `SExtractor` source detection threshold was set at a signal-to-noise ratio (S/N) of S/N > 10 for the Y1 exposures, while for Y2 this threshold was lowered to S/N > 5 (the impact of this change on the stellar completeness is discussed in Section 2.2). During the catalog generation process, we flagged problematic images (e.g., CCDs suffering from reflected light, imaging artifacts, point-spread function (PSF) mis-estimation, etc.) and excluded the affected objects from subsequent analyses. The resulting photometric catalogs were ingested into a high-performance relational database system. Throughout the rest of this paper, photometric fluxes and magnitudes refer to `SExtractor` output for the PSF model fit.

Photometric Calibration: Photometric calibration was performed using the stellar locus regression technique (SLR: Ivezić et al. 2004; MacDonald et al. 2004; High et al. 2009; Gilbank et al. 2011; Coupon et al. 2012; Desai et al. 2012; Kelly et al. 2014). Our reference stellar locus was empirically derived from the globally calibrated DES Y1A1 stellar objects in the region of the Y1A1 footprint with the smallest $E(B − V)$ value from the Schlegel et al. (SFD; 1998) interstellar extinction map. We performed a 1″ match on all Y1 and Y2 objects with S/N > 10 observed in *r*-band and at least one other band. We then applied a high-purity stellar selection

based on the weighted average of the spread_model quantity for the matched objects (|wavg_spread_model_r| < 0.003; see below). The average zero point measured in Y1A1, $ZP_{grizY} = \{30.0, 30.3, 30.2, 29.9, 28.0\}$, was assigned to each star as an initial estimate. Starting from this coarse calibration, we began an iterative procedure to fix the color uniformity across the survey footprint. We segmented the sky into equal-area pixels using the HEALPix scheme (Górski et al. 2005). For each $\sim 0.2 \deg^2$ (resolution nside = 128) HEALPix pixel, we chose the DES exposure in each band with the largest coverage and ran a modified version of the Big MACS SLR code (Kelly et al. 2014)[41] to calibrate each star from the reference exposure with respect to the empirical stellar locus. These stars became our initial calibration standards. We then adjusted the zero points of other CCDs so that the magnitudes of the matched detections agreed with the calibration set from the reference exposure. CCDs with fewer than 10 matched stars or with a large dispersion in the magnitude offsets of matched stars ($\sigma_{ZP} > 0.1$ mag) were flagged. For each calibration star, we computed the weighted-average magnitude in each band using these new CCD zero points; this weighted-average magnitude was used as the calibration standard for the next iteration of the SLR. In the first iteration, we assigned SLR zero points to the calibration stars based on the HEALPix pixel within which they reside. In subsequent iterations, we assigned SLR zero points to the calibration stars based on a bi-linear interpolation of their positions onto the HEALPix grid of SLR zero points. After the second iteration, the color zero points were stable at the 1–2 mmag level. The absolute calibration was set against the 2MASS J-band magnitude of matched stars (making use of the stellar locus in color-space), which were de-reddened using the SFD map with a reddening law of $A_J = 0.709 \times E(B - V)_{SFD}$ from Schlafly & Finkbeiner (2011). The resulting calibrated DES magnitudes are thus already corrected for Galactic reddening by the SLR calibration.

Unique Catalog Generation: There is significant imaging overlap within the DES footprint. For our final high-level object catalog, we identified unique objects by performing a $0''5$ spatial match across all five bands. For each unique object, we calculated the magnitude in each filter in two ways: (1) taking the photometry from the single-epoch detection in the exposure with the largest effective depth,[42] and (2) calculating the weighted average (wavg) magnitude from multiple matched detections. During the catalog generation stage, we kept all objects detected in any two of the five filters (this selection is later restricted to the g- and r-band for our dwarf galaxy search). The process of combining catalog-level photometry increases the photometric precision, but does not increase the detection depth.

The resulting Y2Q1 catalog covers $\sim 5100 \deg^2$ in any single band, $\sim 5000 \deg^2$ in both the g- and r-bands, and $\sim 4700 \deg^2$ in all five bands. The coverage of the Y2Q1 data set is shown in Figure 1. The Y2Q1 catalog possesses a median relative astrometric precision of ~ 40 mas per coordinate and a median absolute astrometric uncertainty of ~ 140 mas per coordinate when compared against UCAC-4. The median absolute photometric calibration agrees within $\sim 3\%$ with the de-reddened global calibration solution of Y1A1 in the overlap region in the $griz$ bands. When variations in the reddening law

are allowed, this agreement improves to $\lesssim 1\%$. The color uniformity of the catalog is $\sim 1\%$ over the survey footprint (tested independently with the red sequence of galaxies). The Y2Q1 catalog has a median point-source depth at an S/N = 10 of $g = 23.4$, $r = 23.2$, $i = 22.4$, $z = 22.1$, and $Y = 20.7$.

2.2. Stellar Object Sample

We selected stars observed in both the g- and r-bands from the Y2Q1 unique object catalog following the common DES prescription based on the wavg_spread_model and spreaderr_model morphological quantities (e.g., Chang et al. 2015; Koposov et al. 2015a). Specifically, our stellar sample consists of well-measured objects with |wavg_spread_model_r| < 0.003 + spreaderr_model_r, flags_$\{g, r\}$ < 4, and magerr_psf_$\{g, r\}$ < 1. By incorporating the uncertainty on spread_model, it is possible to maintain high stellar completeness at faint magnitudes while achieving high stellar purity at bright magnitudes. We sacrificed some performance in our stellar selection by using the r-band spread_model, which has a slightly worse PSF than the i-band; however, relaxing the requirement on i-band coverage increased the accessible survey area.

The stellar completeness is the product of the object detection efficiency and the stellar classification efficiency. As described in Section 2.1, different source detection thresholds were applied to the individual Y1 and Y2 exposures, and accordingly, the detection efficiency for faint objects in Y2Q1 varies across the survey footprint. We used a region of the DES Science Verification data set (SVA1), imaged to full survey depth (i.e., ~ 10 overlapping exposures in each of $grizY$), to estimate the object detection completeness using the individual Y1 exposures. For the Y2 exposures, we instead compared to publicly available catalogs from the Canada–France–Hawaii Telescope Lensing Survey (CFHTLenS; Erben et al. 2013). In both cases, the imaging for the reference catalog is ~ 2 mag deeper than the Y2Q1 catalog. These comparisons show that the Y2Q1 object catalog is >90% complete at about 0.5 mag brighter than the S/N = 10 detection limit.

We estimated the stellar classification efficiency by comparing to CFHTLenS and by using statistical estimates from the Y2Q1 data alone. For the CFHTLenS matching, we identified probable stars in the CFHTLenS catalog using a combination of the class_star output from SExtractor and the fitclass output from the lensfit code (Heymans et al. 2012). Specifically, our CFHTLenS stellar selection was (fitclass = 1) OR (class_star > 0.98), and our galaxy selection was (fitclass = 0) OR (class_star < 0.2). Comparing against the DES stellar classification based on spread_model, we found that the Y2Q1 stellar classification efficiency exceeds 90% for $r < 23$ mag, and falls to $\sim 80\%$ by $r = 24$ (Figure 2). We independently estimated the stellar classification efficiency by creating a test sample of Y2Q1 objects with high stellar purity using the color-based selection $r - i > 1.7$. We then applied the spread_model morphological stellar selection to evaluate the stellar completeness for the test sample. The stellar selection efficiency determined by the color-based selection test is in good agreement with that from the CFHTLenS comparison.

For a typical field at high Galactic latitude, the stellar purity is $\sim 50\%$ at $r = 22.5$ mag, and falls to $\sim 10\%$ at the faint magnitude limit (Figure 2). In other words, the majority of faint objects in the "stellar sample" are misclassified galaxies rather

---

[41] https://code.google.com/p/big-macs-calibrate/
[42] The effective depth is calculated from the exposure time, sky brightness, seeing, and atmospheric transmission (Neilsen et al. 2015).
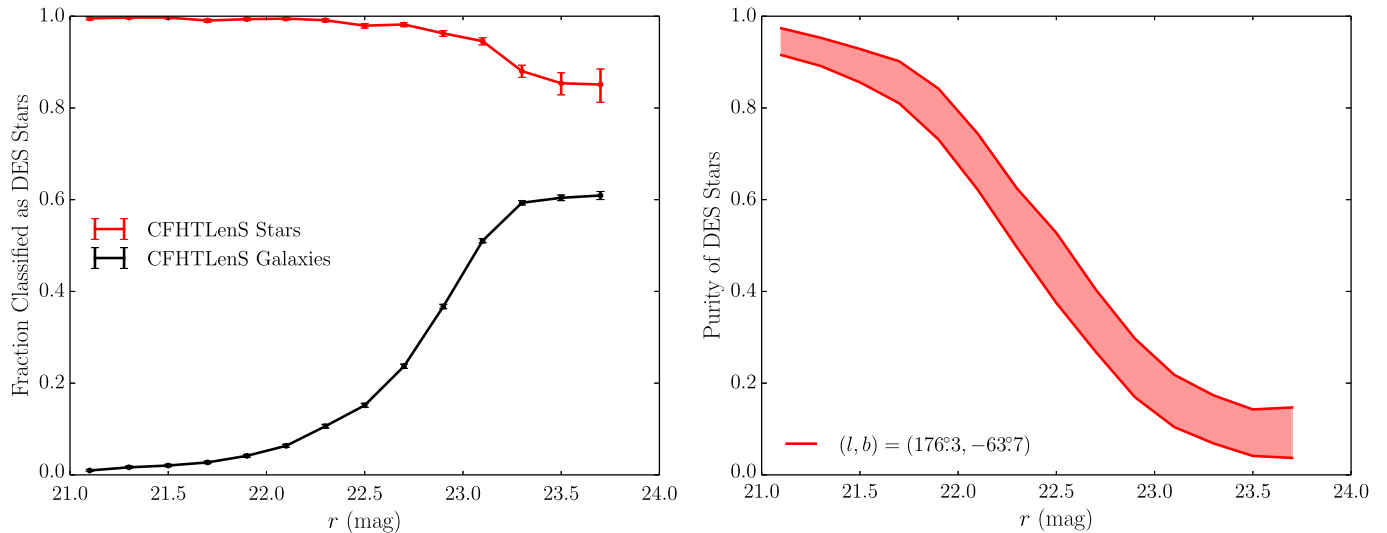
Figure 2. Performance of the morphological stellar classification based on |wavg_spread_model_r| < 0.003 + spreaderr_model_r was evaluated by comparing against deeper CFHTLenS imaging (Section 2.2). Left: fraction of CFHTLenS-classified stars and galaxies that pass our DES stellar selection criteria. Right: stellar purity evaluated in a typical high-Galactic latitude field centered at Galactic coordinates $(l, b) = (176°3, -63°7)$. The shaded region represents the uncertainty associated with objects that are not confidently classified as either stars or galaxies with CFHTLenS. If a large fraction of these ambiguous objects are true stars, the inferred stellar purity for DES is near the upper bound of the indicated range.

than foreground halo stars.[43] This transition can be seen in the color–magnitude distribution diagnostic plots for individual candidates (Section 6.1).

3. SEARCH METHODS

In this section we describe three complementary search strategies that were used to identify overdensities of individually resolved stars matching the old and metal-poor populations that are characteristic of ultra-faint galaxies. Each technique used a different method to estimate the spatially varying field density and to select potential satellite member stars. The output of each search method was a set of seed coordinates, $(\alpha_{2000}, \delta_{2000}, m - M)$, corresponding to statistical excesses relative to the local field density. These seeds were cross-matched between methods and examined in greater detail (Section 5).

When searching for new stellar systems, each detection algorithm applied a deep magnitude threshold ($g < 23.5$ mag or $g < 24$ mag depending on the search technique). At these faint magnitudes, our stellar sample is far from complete (Section 2.2). However, real stellar systems are dominated by faint stars, and the signal-to-noise ratio for satellite discovery can increase by including objects that are fainter than the stellar completeness limit. After candidate systems were identified, we applied a brighter magnitude threshold ($g < 23$ mag) to avoid biasing the fit results during object characterization (Section 5).

One potential concern when extending our search to very faint magnitudes is the increased contamination from misclassified galaxies (Section 2.2). However, as long as the contaminating objects have a similar statistical distribution in the target region and the surrounding area, each technique naturally incorporates the increased object density into the background estimate. There are situations where the assumption of uniformity does not apply (e.g., clusters of galaxies, variations in survey depth, gaps in coverage, etc.); therefore,

when assembling our candidate list, we also examined the distribution of probable galaxies as well as stars with colors far from the expected isochrone (Section 5).

We briefly describe our three search strategies below.

3.1. Stellar Density Maps

Our most straightforward and model-independent search technique used a simple isochrone filter to facilitate visual inspection of the stellar density field. The specific algorithm was a variant of the general approach described in Section 3.1 of Bechtol et al. (2015) and follows from the methods of Koposov et al. (2008), Walsh et al. (2009), and Kim & Jerjen (2015a).

We first increased the contrast of putative satellite galaxies by selecting stars that were consistent with the isochrone of an old ($\tau = 12$ Gyr) and metal-poor ($Z = 0.0001$) stellar population (Dotter et al. 2008). Specifically, we selected stars within 0.1 mag of the isochrone locus in color–magnitude space, enlarged by the photometric measurement uncertainty of each star added in quadrature. After isochrone filtering, we smoothed the stellar density field with a 2′ Gaussian kernel. For each density peak in the smoothed map, we scanned over a range of radii (1′–18′) and computed the Poisson significance of finding the observed number of stars within each circle centered on the density peak given the local field density. This process was repeated for stellar populations at a range of distance moduli (16 mag ⩽ $m - M$ ⩽ 24 mag) and diagnostic plots were automatically generated for each unique density peak. Our nominal magnitude threshold for this search was $g < 24$ mag; however, in regions on the periphery of the survey with large variations in coverage we used a brighter threshold of $g < 23$ mag.

3.2. Matched-filter Search

Our second search strategy utilized a matched-filter algorithm (Balbinot et al. 2011, 2013; Luque et al. 2015). We began by binning objects in our stellar sample with 17 mag

---

[43] This conclusion differs from that of Koposov et al. (2015a), who state that low levels of contamination are observed to the magnitude limit of DES.

$< g < 24$ mag into $1' \times 1'$ spatial pixels and g versus $g-r$ color–magnitude bins of 0.01 mag $\times$ 0.05 mag. We then created a grid of possible simple stellar populations modeled with the isochrones of Bressan et al. (2012) and populated according to a Chabrier (2001) initial mass function to use as signal templates. The model grid spanned a range of distances (10 kpc $< D <$ 200 kpc), ages ($9 < \log_{10} \tau < 10.2$), and metallicities ($Z$ = {0.0002, 0.001, 0.007}). The color–magnitude distribution of the field population was empirically determined over larger $10° \times 10°$ regions. For each isochrone in the grid, we then fit the normalization of the simple stellar population in each spatial pixel to create a corresponding density map for the full Y2Q1 area.

The set of pixelized density maps do not assume a spatial model for the stellar system, and can be used to search for a variety of stellar substructures (e.g., streams and diffuse clouds). To search specifically for dwarf galaxies, we convolved the density maps with Gaussian kernels having widths ranging from $0'$ (no convolution) to $9'$ and used SExtractor to identify compact stellar structures in those maps. This convolution and search was performed on each map for our grid of isochrones. The resulting seeds were ranked according to their statistical significance and by the number of maps in which they appeared, i.e., the number of isochrones for which an excess was observed.

3.3. Likelihood-based Search

Our third search technique was a maximum-likelihood-based algorithm that simultaneously used the full spatial and color–magnitude distribution of stars, as well as photometric uncertainties and information about the survey coverage. The likelihood was constructed from the product of Poisson probabilities for detecting each individual star given its measured properties and the parameters that describe the field population and putative satellite (Section 3.2 of Bechtol et al. 2015). When searching for new stellar systems, we used a spherically symmetric Plummer model as the spatial kernel, and a composite isochrone model consisting of four isochrones of different ages, τ = {12 Gyr, 13.5 Gyr}, and metallicities, Z = {0.0001, 0.0002}, to bracket a range of possible stellar populations (Bressan et al. 2012). We scanned the Y2Q1 data testing for the presence of a satellite galaxy at each location on a multi-dimensional grid of sky position ($0\overset{.}{'}7$ resolution; HEALPix nside = 4096), distance modulus (16 mag $< m - M$ < 23 mag), and kernel half-light radius ($r_{\rm h}$ = {$0\overset{.}{°}03$, $0\overset{.}{°}1$, $0\overset{.}{°}3$}). For the likelihood search, we restricted our magnitude range to 16 mag $< g < 23.5$ mag as a compromise between survey depth and stellar completeness. The statistical significance of a putative galaxy at each grid point was expressed as a test statistic (TS) based on the likelihood ratio between a hypothesis that includes a satellite galaxy versus a field-only hypothesis (Equation (4) of Bechtol et al. 2015). As a part of the model fitting, the satellite membership probability is computed for every star in the region of interest. These photometric membership probabilities can be used to visualize which stars contribute to the candidate detection significance (Section 5) and have previously been used to select targets for spectroscopic follow-up (Simon et al. 2015; Walker et al. 2015).

4. CANDIDATE SELECTION

The search methods described in Section 3 each produced a set of seed locations (α_{2000}, δ_{2000}, $m - M$) for overdensities in the stellar field and a significance associated with each seed. Before performing a computationally intensive multi-parameter likelihood fit to characterize each seed, we applied a set of simple selection cuts to remove seeds that are unlikely to be new Milky Way satellites. We set detection significance thresholds at $>5.5\sigma$ for the stellar density map search and TS > 45 ($\sim 6\sigma$) for the maximum-likelihood search. For the matched-filter method, the ten highest-ranked seeds were selected from each $10° \times 10°$ search region. After thresholding, the union of all three search techniques yielded several hundred unique seeds. Many of these seeds were attributed to steep gradients in the stellar density field, numerical effects near the survey boundaries, and imaging artifacts. We also compared against catalogs of other astrophysical objects that produce false positives, such as large nearby galaxies (Nilson 1973; Corwin 2004) and galaxy clusters (Rykoff et al. 2014). These objects were removed from our list of candidates and we did not pursue investigation at lower significance thresholds due to an increased false positive rate.

The resulting list of seeds was matched against catalogs of known Local Group galaxies (McConnachie 2012) and star clusters (Harris 1996, 2010 edition; Kharchenko et al. 2013). Some of the most prominent stellar systems in our list of seeds were the Fornax, Phoenix, Sculptor,[44] and Tucana dwarf galaxies, and the globular clusters AM 1, Eridanus, Reticulum, Whiting 1, NGC 288, NGC 1261, NGC 1851, NGC 1904, and NGC 7089. Additionally, seed locations were compared against other stellar overdensities recently reported in the DES footprint (Bechtol et al. 2015; Kim et al. 2015b; Koposov et al. 2015a; Kim & Jerjen 2015b; Luque et al. 2015) and all 11 objects were recovered with high significance. The locations of previously known stellar systems in the DES footprint are shown in Figure 3.

As an additional test of the physical nature of the ~ 30 highest significance unassociated seeds, we explored the posterior probability density of the likelihood with an affine invariant Markov Chain Monte Carlo (MCMC) ensemble sampler (MCMC; Foreman-Mackey et al. 2013).[45] This step was meant as a preliminary investigation of whether the posterior distribution was well-constrained by the data. We fixed the distance modulus of each object at the value that maximized the likelihood in the grid search (Section 16) and sampled the morphological parameters (center position, extension, ellipticity, and position angle) along with the richness of the putative stellar system. We imposed a Jeffreys' prior on the extension ($\mathcal{P}(a_{\rm h}) \propto 1/a_{\rm h}$) and flat priors on all other parameters. The posterior probability was sampled with 2.5×10^5 steps and we rejected seeds that lacked a well-defined maximum in the posterior.

The process described above resulted in the selection of eight candidate stellar systems. Six of these candidates, DES J2204–4626 (Gru I), DES J2356–5935 (Tuc III), DES J0531–2801 (Col I), DES J0002–6051 (Tuc IV), DES J0345–6026 (Ret III), and DES J2337–6316 (Tuc V), are high-confidence detections in clean regions of the survey. The additional two candidates,

---

[44] The center of Sculptor lies in a hole in Y2Q1 coverage, though the outskirts are still detected at high significance.
[45] emcee v2.1.0: http://dan.iel.fm/emcee/

Figure 3. Cartesian projection of the density of stars observed in both the *g*- and *r*-bands with *g* < 23 and *g* − *r* < 1 over the DES Y2Q1 footprint (∼5000 deg²). Globular clusters are marked with "+" symbols (Harris 1996, 2010 edition), two faint outer halo clusters are marked with "×" symbols (Kim et al. 2015b; Luque et al. 2015), Local Group galaxies known prior to DES are marked with blue squares (McConnachie 2012), dwarf galaxy candidates discovered in Y1 DES data are marked with red outlined circles, and the Y2 stellar systems are marked with red triangles. The periphery of the LMC can be seen in the southeast corner of the footprint, while the Galactic stellar disk can be seen on the eastern and western edges.

Table 1
Detection of Ultra-faint Galaxy Candidates

Name	α_{2000} (deg)	δ_{2000} (deg)	$m - M$	r_h (′)	a_h (′)	ϵ	ϕ	Map Sig. (σ)	TS Scan	$\sum p_i$
DES J2204−4626 (Gru II)	331.02	−46.44	18.62 ± 0.21	$6.0^{+0.9}_{-0.5}$	…	<0.2	…	15.7	369	161
DES J2356−5935 (Tuc III)[a]	359.15	−59.60	17.01 ± 0.16	$6.0^{+0.8}_{-0.6}$	…	…	…	11.1	390	168
DES J0531−2801 (Col I)[b]	82.86	−28.03	21.30 ± 0.22	$1.9^{+0.5}_{-0.4}$	…	<0.2	…	10.5	71	33
DES J0002−6051 (Tuc IV)	0.73	−60.85	18.41 ± 0.19	$9.1^{+1.7}_{-1.4}$	$11.8^{+2.2}_{-1.8}$	$0.4^{+0.1}_{-0.1}$	11 ± 9	8.7	287	134
DES J0345−6026 (Ret III)[b]	56.36	−60.45	19.81 ± 0.31	$2.4^{+0.9}_{-0.8}$	…	<0.4	…	8.1	56	22
DES J2337−6316 (Tuc V)	354.35	−63.27	18.71 ± 0.34	$1.0^{+0.3}_{-0.3}$	$1.8^{+0.5}_{-0.6}$	$0.7^{+0.1}_{-0.2}$	30 ± 5	8.0	129	24
DES J2038−4609 (Ind II)[b]	309.72	−46.16	21.65 ± 0.16	$2.9^{+1.1}_{-1.0}$	…	<0.4	…	6.0	32	22
DES J0117−1725 (Cet II)	19.47	−17.42	17.38 ± 0.19	$1.9^{+1.0}_{-0.5}$	…	<0.4	…	5.5	53	21

Notes. Characteristics of satellite galaxy candidates discovered in DES Y2 data. Best-fit parameters from the maximum-likelihood analysis assume a Bressan et al. (2012) isochrone. Uncertainties come from the highest density interval containing 68% of the posterior distribution. The uncertainty on the distance modulus (*m* − *M*) also includes systematic uncertainties coming from the choice of theoretical isochrone and photometric calibration (Section 5). The azimuthally averaged half-light radius (r_h) is quoted for all candidates. For systems with evidence for asphericity (Bayes' factor > 3), we quote the ellipticity (ϵ), the position angle (ϕ), and the length of the semimajor axis of the ellipse containing half of the light ($a_\mathrm{h} = r_\mathrm{h}/\sqrt{1-\epsilon}$). Upper limits on the ellipticity are quoted for other candidates at 84% confidence. "Map Sig." refers to detection significance of the candidate from the stellar density map search method (Section 3.1). "TS Scan" refers to the significance (Equation (4) in Bechtol et al. 2015) from the likelihood scan (Section 3.3). $\sum p_i$ is the estimated number of satellite member stars in the DES Y2Q1 catalog with *g* < 23 mag.
[a] Fit with a spherically symmetric Plummer profile due to the possible presence of tidal tails (Section 6.1).
[b] Fit with a composite isochrone: τ = {12 Gyr, 13.5 Gyr}, Z = {0.0001, 0.0002} (Section 5).

DES J2038−4609 (Ind II) and DES J0117−1725 (Cet II), are lower confidence and reside in more complicated regions. In Table 1 we report the coordinates and detection significances of each of these objects.

5. CANDIDATE CHARACTERIZATION

In this section, we describe the iterative procedure used to characterize each of the eight candidate stellar systems. When fitting the new candidates, we applied a brighter magnitude threshold, *g* < 23 mag, to mitigate the impact of stellar incompleteness. The results of our characterization are shown in Tables 1 and 2.

We began by simultaneously fitting the morphological parameters and distance modulus of each candidate following the procedure described in Section 4. Best-fit values were derived from the marginalized posterior distribution and the morphological parameters were temporarily fixed at these values. We then ran a MCMC chain simultaneously sampling the distance, age, metallicity, and richness, assuming flat priors on each parameter. Significant correlations between these parameters were found, and in some cases the age and metallicity were poorly constrained (see below). To assess the error contribution from intrinsic uncertainty in the isochrone, we resample the posterior distribution using the Dartmouth isochrone family (Dotter et al. 2008). In general, the best-fit distance moduli agree to within 0.1 mag when the data were fit

Table 2
Derived Properties of Ultra-faint Galaxy Candidates

Name	ℓ (deg)	b (deg)	Distance (kpc)	M_* ($10^3\,M_\odot$)	M_V (mag)	$r_{1/2}$ (pc)	τ (Gyr)	Z
DES J2204–4626 (Gru II)	351.15	−51.94	53 ± 5	$3.4^{+0.3}_{-0.4}$	−3.9 ± 0.22	93 ± 14	12.5	0.0002
DES J2356–5935 (Tuc III)[a]	315.38	−56.19	25 ± 2	$0.8^{+0.1}_{-0.1}$	−2.4 ± 0.42	44 ± 6	10.9	0.0001
DES J0531–2801 (Col I)[b]	231.62	−28.88	182 ± 18	$6.2^{+1.9}_{-1.0}$	−4.5 ± 0.17	103 ± 25	…	…
DES J0002–6051 (Tuc IV)	313.29	−55.29	48 ± 4	$2.2^{+0.4}_{-0.3}$	−3.5 ± 0.28	127 ± 24	11.6	0.0001
DES J0345–6026 (Ret III)[b]	273.88	−45.65	92 ± 13	$2.0^{+0.6}_{-0.7}$	−3.3 ± 0.29	64 ± 24	…	…
DES J2337–6316 (Tuc V)	316.31	−51.89	55 ± 9	$0.5^{+0.1}_{-0.1}$	−1.6 ± 0.49	17 ± 6	10.9	0.0003
DES J2038–4609(Ind II)[b]	353.99	−37.40	214 ± 16	$4.9^{+1.8}_{-1.6}$	−4.3 ± 0.19	181 ± 67	…	…
DES J0117–1725 (Cet II)	156.48	−78.53	30 ± 3	$0.1^{+0.04}_{-0.04}$	0.0 ± 0.68	17 ± 7	10.9	0.0002

Notes. Derived properties of the DES Y2 satellite candidates. Stellar masses (M_*) are computed for a Chabrier (2001) initial mass function. The absolute visual magnitude is derived via the procedure of Martin et al. (2008) using the transformation equations from Bechtol et al. (2015). The uncertainty on the azimuthally averaged physical half-light radius ($r_{1/2}$) includes the uncertainty in the projected half-light radius and distance. Age (τ) and metallicity (Z) values come from the peak of the posterior distribution.
[a] Fit with a spherically symmetric Plummer profile due to the possible presence of tidal tails (Section 6.1).
[b] Fit with a composite isochrone: $\tau = \{12\,\text{Gyr}, 13.5\,\text{Gyr}\}$, $Z = \{0.0001, 0.0002\}$ (Section 5).

by these two isochrone classes. To determine the uncertainty on the distance modulus quoted in Table 1 we started with the highest posterior density interval from the Bressan et al. (2012) isochrone fit. We then calculated a systematic component from the difference in the best-fit distance modulus derived with Bressan et al. (2012) and Dotter et al. (2008) isochrones. An additional ±0.03 mag uncertainty was added to account for uncertainty in the photometric calibration. The age and metallicity values were taken from the peak of the marginalized posterior density from the Bressan et al. (2012) isochrone fit.

For the distant systems (i.e., DES J0531–2801, DES J2038–4609, and DES J0345–6026), the main-sequence turnoff (MSTO) is fainter than the $g < 23$ mag limit imposed for our fit. In these systems, the data provide weaker constraints on the age and metallicity. We therefore fit the distance modulus using a composite of four Bressan et al. (2012) isochrones with fixed ages, $\tau = \{12\,\text{Gyr}, 13.5\,\text{Gyr}\}$, and metallicities, $Z = \{0.0001, 0.0002\}$. We followed the procedure above to incorporate systematic uncertainties from the choice of theoretical isochrone family and from the calibration.[46]

Fixing the distance, age, and metallicity at the values derived in the previous step, we then re-fit the morphological parameters. The best-fit values of the morphological parameters and their highest posterior density intervals are listed in Table 1. The majority of objects show no significant evidence for ellipticity, which is confirmed by calculating the Bayes factor (BF) via the Savage–Dickey density ratio (Dickey 1971; Trotta 2007). For objects with evidence for asphericity (BF > 3), we report both the elliptical Plummer radius, a_h, and the position angle, ϕ. For all objects, we report the azimuthally averaged half-light radius, r_h. In the region of DES J2356–5935 there is a linear structure visible in the filtered stellar density map, consistent with a set of tidal tails (Section 6.1). We require the spatial profile of DES J2356–5935 to be azimuthally symmetric in the MCMC fit and analyze this linear feature separately.

The best-fit parameters derived from our iterative MCMC analysis along with several additional derived properties are

reported in Tables 1 and 2. The physical size of each object was calculated by propagating the uncertainty from the distance and azimuthally averaged half-light radius. Absolute magnitudes were calculated according to the prescription of Martin et al. (2008) and do not include the distance uncertainty.

The two lower-confidence candidates are located in complicated regions of the survey. DES J0117–1725 is located in a region of sparse coverage and is close to both a CCD chip gap and a larger hole in the survey. DES J2038–4609 is located in a region of non-uniform depth at the interface of Y1 and Y2 observations. Although we have attempted to account for these issues in the likelihood fit, we caution that the parameters derived for these systems may be less secure than for the other candidates.

As a final note, the iterative MCMC fitting procedure described above was also applied to the satellite galaxy candidate Grus I (Koposov et al. 2015a). Grus I was identified in Y1A1 imaging data, but was located close to a CCD chip gap in a region with sparse coverage. We reanalyzed Grus I with the additional Y2 exposures and found that its structural parameters are consistent within uncertainties with those reported by Koposov et al. (2015a).

6. DISCUSSION

Spectroscopic observations are needed to definitively classify the newly discovered stellar systems as either star clusters or ultra-faint dwarf galaxies based upon their stellar dynamics and/or metallicity dispersions. However, the distances, physical sizes, and luminosities derived from DES photometry (Table 2) already suggest a galactic classification for many of the new candidates. In Figures 4 and 5, we show the distributions of physical half-light radius heliocentric distance versus absolute magnitude for Milky Way globular clusters (Harris 1996, 2010 edition) and Local Group galaxies (McConnachie 2012). We find that all of the systems discovered in Y2Q1 fall along the established locus for nearby galaxies. Several of the new systems possess lower surface brightnesses than any confirmed ultra-faint galaxy,[47] supporting earlier conclusions that the threshold in surface brightness was an observational selection effect (Koposov et al. 2008;

---

[46] One notable exception is the case of DES J2038–4609, where significant constraining power comes from a set of horizontal branch (HB) stars. For DES J2038–4609 we estimated the distance uncertainty from the Bressan et al. (2012) isochrone analysis alone.

[47] A potential exception to this statement is the large, faint, and perhaps tidally disrupted object Böotes III (Carlin et al. 2009).
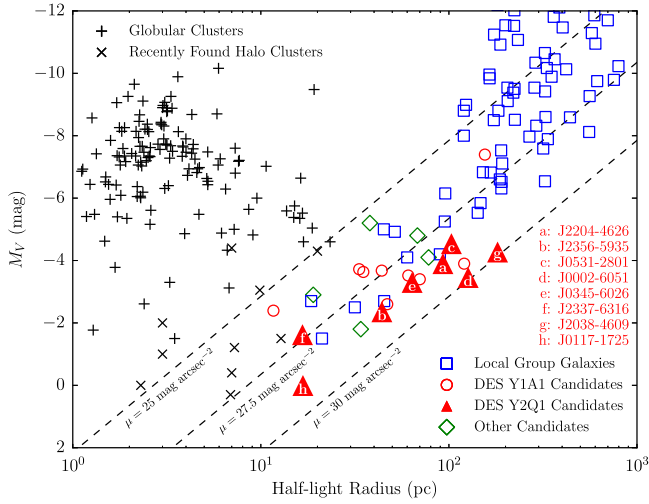
Figure 4. Local Group galaxies (McConnachie 2012) and globular clusters (Harris 1996, 2010 edition) occupy distinct regions in the plane of physical half-light radius (azimuthally averaged) and absolute magnitude. The majority of DES satellite candidates (red triangles and circles) are more consistent with the locus of Local Group galaxies (blue squares) than with the population of Galactic globular clusters (black "+"). Other recently reported dwarf galaxy candidates (green diamonds) include Hydra II (Martin et al. 2015), Triangulum II (Laevens et al. 2015b), Pegasus III (Kim et al. 2015a), Draco II, and Sagittarius II (Laevens et al. 2015a). Several outer halo star clusters and systems of ambiguous classification are indicated with "×" symbols: Koposov 1 and Koposov 2 (Koposov et al. 2007; Paust et al. 2014), Segue 3 (Belokurov et al. 2010; Fadely et al. 2011; Ortolani et al. 2013), Muñoz 1 (Muñoz et al. 2012), Balbinot 1 (Balbinot et al. 2013), Laevens 1 (Belokurov et al. 2014; Laevens et al. 2014), Laevens 3 (Laevens et al. 2015a), Kim 1 and Kim 2 (Kim & Jerjen 2015a; Kim et al. 2015b), and DES 1(Luque et al. 2015). The dashed lines indicate contours of constant surface brightness at $\mu = \{25, 27.5, 30\}$ mag arcsec^{-2}.

Walsh et al. 2009). Finally, globular clusters generally have small ellipticities, $\epsilon \lesssim 0.2$ (van den Bergh 2008), while dwarf galaxies are commonly more elliptical (Martin et al. 2008). However, the ellipticities of many of the new objects are not well-constrained by the DES data and thus do not provide a strong indicator of the nature of these objects.

The spatial distribution of the new candidates within the DES footprint is suggestive of an association with the Magellanic Clouds (Section 6.3). When discussing this scenario, the coordinates of the Large Magellanic Cloud (LMC) are taken to be $\alpha_{2000}, \delta_{2000}, D_{\odot} = (80°.89, -69°.76, 49.89 \text{ kpc})$ (distance from de Grijs et al. 2014) and the coordinates of the Small Magellanic Cloud (SMC) are taken to be $(\alpha_{2000}, \delta_{2000}, D_{\odot}) = (13°.19, -72°.83, 61.94 \text{ kpc})$ (distance from de Grijs & Bono 2015).[48] While the new DES candidates reside in a region close to the Magellanic Stream, no candidate is found to be coincident with the main filament of the Stream. A similar observation was made by Koposov et al. (2015a) for the DES stellar systems discovered in Y1.

We also investigate a potential group of satellites in the constellation Tucana, consisting of DES J0002–6051 and DES J2337–6316, and the object DES J2251.2–5836 (Tuc II) discovered in Y1 data (Bechtol et al. 2015; Koposov et al. 2015a). The centroid of the Tucana group is at $(\alpha_{2000}, \delta_{2000}, D_{\odot}) = (351°.90, -61°.06, 53.63 \text{ kpc})$, and the separation of each member from the centroid is $\lesssim 7$ kpc (Table 3). This grouping of objects is projected onto a region of H I gas that is

---

[48] Sky coordinates taken from NED: https://ned.ipac.caltech.edu

Table 3
Physical Separations of Ultra-faint Galaxy Candidates

Name	$D_{\odot}$ (kpc)	D_{GC} (kpc)	D_{LMC} (kpc)	D_{SMC} (kpc)	D_{Tuc} (kpc)
DES J2204–4626 (Gru II)	53	49	46	33	18
DES J2356–5935 (Tuc III)	25	23	32	38	28
DES J0531–2801 (Col I)	182	186	149	157	168
DES J0002–6051 (Tuc IV)	48	46	27	18	7
DES J0345–6026 (Ret III)	92	92	45	40	53
DES J2337–6316 (Tuc V)	55	52	29	14	3
DES J2038–4609 (Ind II)	214	208	193	170	169
DES J0117–1725 (Cet II)	30	32	46	51	40
DES J2251.2–5836 (Tuc II)	58	54	37	20	7

Note. Three-dimensional physical separation between DES satellite candidates and the LMC and SMC. Also listed is the heliocentric distance, the Galactocentric distance, and the separation to the centroid of the proposed Tucana group comprising DES J2251.2–5836, DES J0002–6051, and DES J2337–6316.
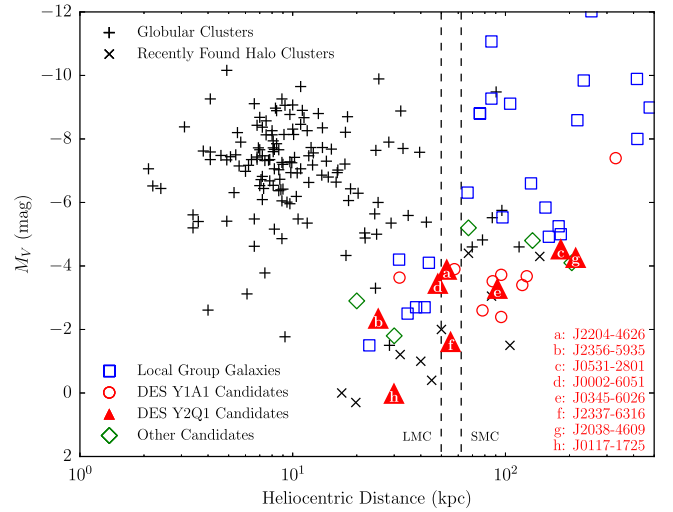
Figure 5. DES satellite galaxy candidates (red circles and triangles) have comparable luminosities to known Local Group galaxies (blue squares; McConnachie 2012) and other newly discovered galaxy candidates (green diamonds), but are typically found at larger distances. The dashed lines indicate the heliocentric distances of the LMC and SMC. Globular clusters (black "+" symbols, Harris 1996) and outer halo star clusters ("×" symbols) have been detected at comparable luminosities and distances due to their more compact nature. The constituents of each source class can be found in Figure 4.

likely a secondary filament or high-velocity cloud associated with the head of the Magellanic Stream (Putman et al. 2003; McClure-Griffiths et al. 2009).

6.1. Review of Individual Candidates

1. *DES J2204–4626* (Grus II, Figure 6): As the most significant new candidate, DES J2204–4626 has ∼161 probable member stars with $g < 23$ mag in the DES imaging. The large physical size of this system (93 pc) allows it to be tentatively classified as an ultra-faint dwarf galaxy. A clear red giant branch (RGB) and MSTO are seen in the color–magnitude diagram of DES J2204–4626. Several likely blue horizontal branch (BHB) members are seen at $g \sim 19$ mag. There is a small gap in survey coverage ∼0°.5 from the centroid of
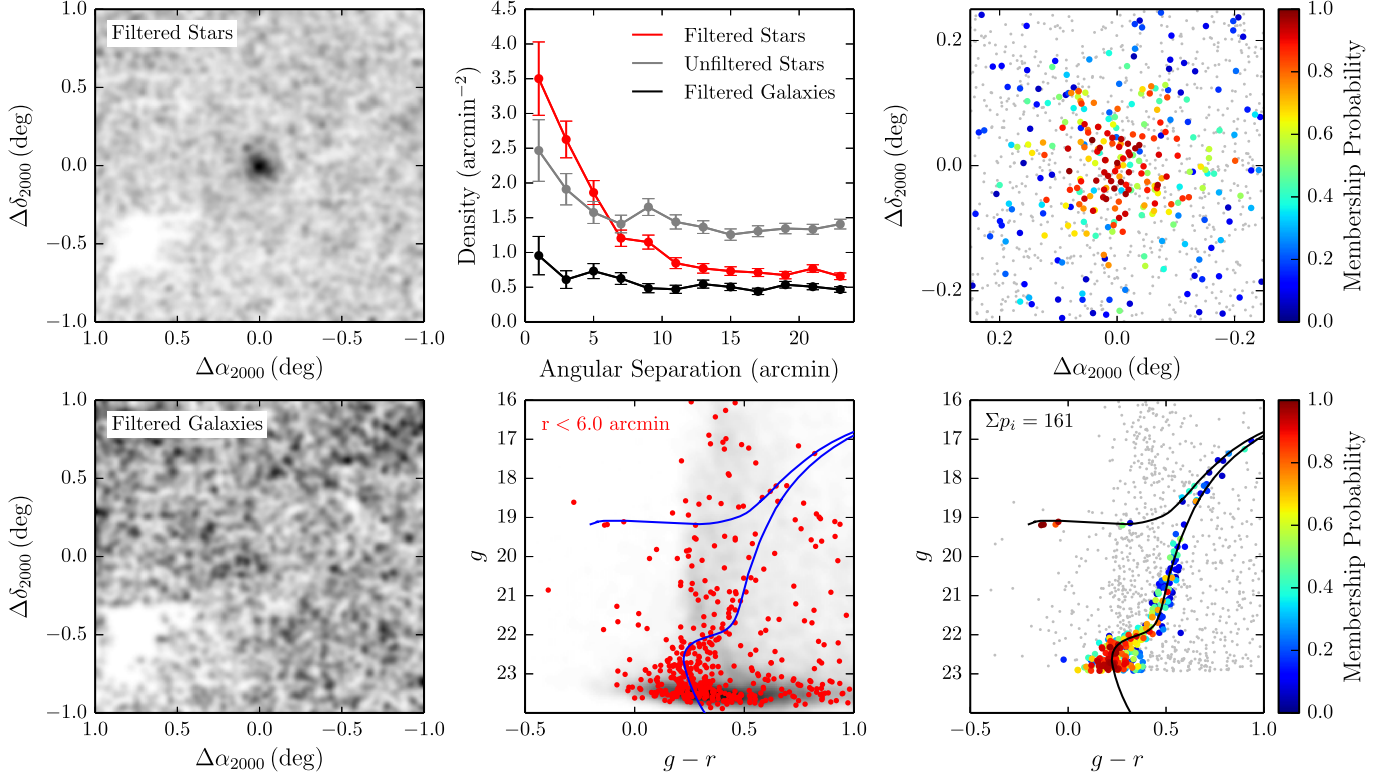
DES J2204-4626 (Grus II); $(\alpha_{2000}, \delta_{2000}, m - M) = (331°.02, -46°.44, 18.62)$

Figure 6. Stellar density and color–magnitude diagrams for DES J2204–4626 (Grus II). Top left: spatial distribution of stellar objects with $g < 24$ mag that pass the isochrone filter (see text). The field of view is $2° \times 2°$ centered on the candidate and the stellar distribution has been smoothed by a Gaussian kernel with standard deviation $1'.2$. Top center: radial distribution of objects with $g - r < 1$ mag and $g < 24$ mag: stars passing the isochrone filter (red), stars excluded from the isochrone filter (gray), and galaxies passing the isochrone filter (black). Top right: spatial distribution of stars with high membership probabilities within a $0°.5 \times 0°.5$ field of view. Small gray points indicate stars with membership probability less than 5%. *Bottom left*: same as top left panel, but for probable galaxies that pass the isochrone filter. Bottom center: the color–magnitude distributions of stars within $0°.1$ of the centroid are indicated with individual points. The density of the field within an annulus from radii of $0°.5–1°.0$ is represented by the background two-dimensional histogram in grayscale. The blue curve shows the best-fit isochrone as described in Tables 1 and 2. Bottom right: color–magnitude distribution of high membership probability stars.

DES J2204–4626, but this is accounted for in the maximum-likelihood analysis and should not significantly affect the characterization of this rich satellite.

DES J2204–4626 is from the LMC (46 kpc) and from the Galactic center (49 kpc). It is slightly closer to the SMC (33 kpc) and intriguingly close to the the group of stellar systems in Tucana (∼18 kpc). While it is unlikely that DES J2204–4626 is currently interacting with any of the other known satellites, we cannot preclude the possibility of a past association.

2. *DES J2356–5935* (Tucana III, Figure 7): DES J2356–5935 is another highly significant stellar system that presents a clearly defined main sequence and several RGB stars. The physical size and luminosity of DES J2356–5935 ($r_{1/2} = 44$ pc, $M_V = -2.4$ mag) are comparable to that of the recently discovered dwarf galaxy Reticulum II. At a distance of 25 kpc, DES J2356–5935 would be among the nearest ultra-faint satellite galaxies known, along with Segue 1 (23 kpc), Reticulum II (32 kpc), and Ursa Major II (32 kpc). The relative abundance of bright stars in DES J2356–5935 should allow for an accurate spectroscopic determination of both its velocity dispersion and metallicity. DES J2356–5935 is reasonably close to the LMC and SMC (32 kpc and 38 kpc, respectively), and

measurements of its systemic velocity will help to elucidate a physical association.

As mentioned in Section 5, there is an additional linear feature in the stellar density field around DES J2356–5935 that strongly influences the fitted ellipticity of this galaxy candidate. In Figure 8, we show the $6° \times 6°$ region centered on DES J2356–5935, which contains this linear feature. Selecting stars with the same isochrone filter used to increase the contrast of DES J2356–5935 relative to the field population, we found a faint stellar overdensity extending ∼2° on both sides of DES J2356–5935. This feature has an FWHM of ∼0°.3 (i.e., projected dimensions of 1.7 kpc × 130 pc at a distance of 25 kpc) and is oriented ∼85° east of north. The length of the feature and the smooth density field observed with an inverted isochrone filter support the conclusion that this is a genuine stellar structure associated with DES J2356–5935.

One interpretation is that DES J2356–5935 is in the process of being tidally stripped by the gravitational potential of the Milky Way. The relatively short projected length of the putative tails may imply that DES J2356–5935 is far from its orbital pericenter (where tidal effects are strongest) and/or that stripping began recently. Despite the possible presence of tidal tails, the

DES J2356-5935 (Tucana III); $(\alpha_{2000}, \delta_{2000}, m - M) = (359°15, -59°60, 17.01)$
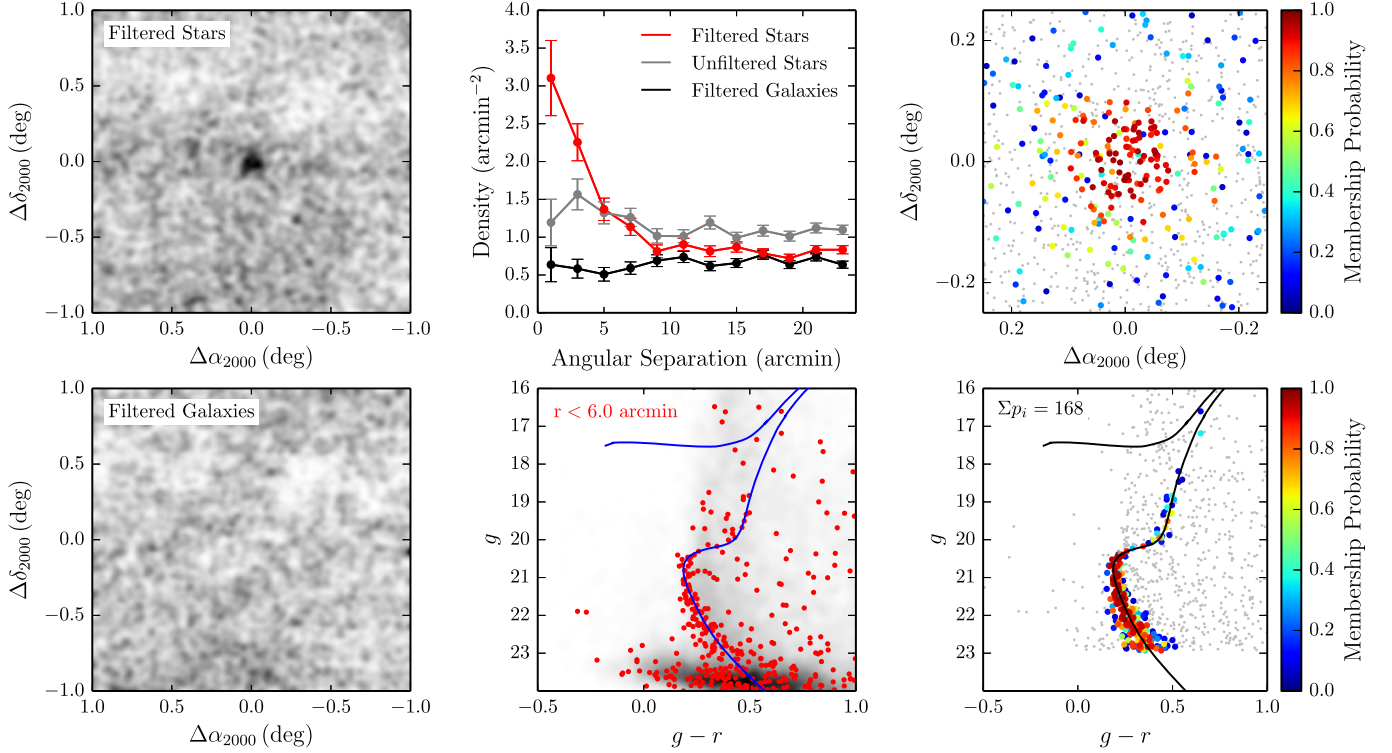
Figure 7. Analogous to Figure 6 but for DES J2356–5935 (Tucana III).

main body of DES J2356–5935 appears to be relatively round. While the proximity of DES J2356–5935 might make it an important object for indirect dark matter searches, evidence of tidal stripping would suggest that a large fraction of its outer dark matter halo has been removed. However, the mass within the stellar core (and therefore the dark matter content in the central region) can still likely be determined accurately (Oh et al. 1995; Muñoz et al. 2008; Peñarrubia et al. 2008).

3. *DES J0531–2801* (Columba I, Figure 9): DES J0531–2801 is the second most distant of the Y2 DES candidates (182 kpc) and is detected as a compact cluster of RGB stars. Both the BHB and red horizontal branch (RHB) appear to be well-populated. The distance, physical size (103 pc), and luminosity ($M_V = -4.5$ mag) of DES J0531–2801 place it in the locus of Local Group dwarf galaxies, comparable to Leo IV and CVn II (Belokurov et al. 2007). DES J0531–2801 is isolated from the other new DES systems and is likely not associated with the Magellanic system.

4. *DES J0002–6051* (Tucana IV, Figure 10): DES J0002–6051 has the largest angular size of the candidates ($r_h = 9.1$), which at a distance of 48 kpc corresponds to a physical size of $r_{1/2} \sim 127$ pc. This large half-light radius is inconsistent with the sizes of known globular clusters (Harris 1996, 2010 edition), thus making it very likely that DES J0002–6051 is a dwarf galaxy. The measured ellipticity of DES J0002–6051, $\epsilon = 0.4$, is also consistent with a galactic classification. DES J0002–6051 is found to be 27 kpc from the LMC and 18 kpc from the SMC. DES J0002–6051 is one of the proposed members of the Tucana group, with a centroid separation of 7 kpc.

Measurements of the radial velocity and proper motion of DES J0002–6051 will provide strong clues as to whether it was accreted as part of a system of satellites. Similar to DES J2356–5935 and DES J2204–4626, the MSTO of DES J0002–6051 is well-populated and clearly visible. Several possible member stars can also be seen along the HB.

5. *DES J0345–6026* (Reticulum III, Figure 11): DES J0345–6026 appears to be similar to DES J2204–4626 in its structural properties, but is more distant (heliocentric distance of 92 kpc). Like DES J2204–4626, DES J0345–6026 can be tentatively classified as a dwarf galaxy based on its physical size and low surface brightness. There is some indication of asphericity for this object; however, the ellipticity is not significantly constrained by the DES data. DES J0345–6026 has a sparsely populated RGB, a few possible RHB members, and two possible BHB members. The MSTO for DES J0345–6026 is slightly fainter than our fitting threshold of $g < 23$ mag, thus its age is poorly constrained.

6. *DES J2337–6316* (Tucana V, Figure 12): DES J2337–6316 is the second new system in the Tucana group and is the closest to the group's centroid (3 kpc). At a heliocentric distance of 55 kpc, DES J2337–6316 is also located 29 kpc from the LMC and 14 kpc from the SMC. The physical size (17 pc) and luminosity ($M_V \sim -1.6$ mag) place DES J2337–6316 in a region of the size–luminosity plane close to Segue 1, Willman 1, and Kim 2. Segue 1 and Willman 1 have sizes similar to the most extended globular clusters, but are approximately an order of magnitude less luminous. On the other hand, deep imaging of Kim 2 has led Kim et al. (2015b) to

$$(\alpha_{2000}, \delta_{2000}, m - M) = (359°.15, -59°.60, 17.01)$$
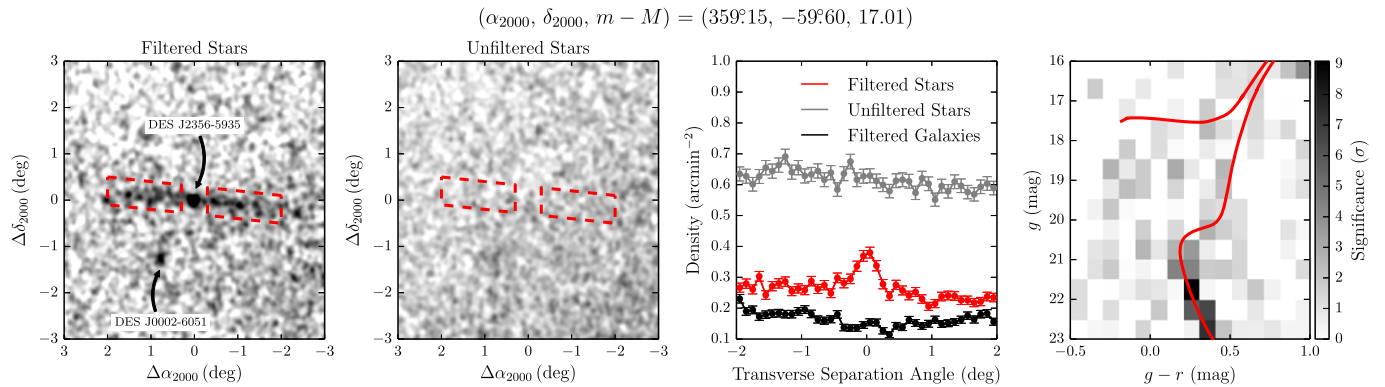
Figure 8. Possible tidal tails around DES J2356–5935 (Tucana III). Left: spatial distribution of stellar objects with $g < 23$ mag that pass the same isochrone filter as applied to visualize DES J2356–5935 (Figure 7). Red boxes highlight the positions of the tidal tails. Middle left: spatial distribution of stellar objects with $g - r < 1$ mag and $g < 23$ mag not passing the isochrone filter. Middle right: average density profiles transverse to the tidal tail axis: stars passing the isochrone filter (red), other unfiltered stars (gray), and galaxies passing the isochrone filter (black). For the density calculation, the range of included angles parallel to the tidal tails is $\pm2°.0$, excluding the region within $0°.3$ of DES J2356–5935. Right: binned significance diagram representing the Poisson probability of detecting the observed number of stars within $0°.2$ of the tidal tail axis (excluding the region within $0°.3$ of DES J2356–5935) for each bin of the color–magnitude space given the local field density.

conclude that it is very likely a star cluster. DES J2337–6316 is one of the few new objects for which the DES data places a constraint on ellipticity. The high ellipticity, $\epsilon = 0.7$, supports a galactic classification for DES J2337–6316. Most of the high probability member stars for DES J2337–6316 are on the main sequence and fainter than $g \sim 22.5$ mag. As with other similarly faint objects, a few stars situated close to the lower RGB are also likely members. A system similar to DES J2337–6316 would have been difficult to detect in SDSS with a threshold at $r < 22$.

7. *DES J2038–4609* (Indus II, Figure 13): DES J2038–4609 is the first of the two lower-confidence candidates. The detection of this object comes predominantly from a tight clump of BHB stars at $g \sim 22$ mag and $g-r \sim 0$ mag. Three of the potential HB members are clustered within a spatial region of radius $\sim10''$. Several additional HB and RGB stars are assigned non-zero membership probabilities by the likelihood fit, enlarging the best-fit size of this system. DES J2038–4609 is located at a boundary between the Y1 and Y2 imaging, and the effect of the deeper Y2 source detection threshold is visible when extending to magnitudes of $g > 23$ mag. The best-fit physical size of DES J2038–4609 (181 pc) would place it among the population of Local Group galaxies. Deeper imaging is needed to better characterize this candidate since the MSTO is fainter than the current DES detection threshold.

8. *DES J0117–1725* (Cetus II, Figure 14): DES J0117–1725 is the second lower-confidence candidate, being the least luminous ($M_V = 0.0 \pm 0.68$ mag) and most compact ($r_{1/2} = 17$ pc) of the new stellar systems. DES J0117–1725 is nearly two orders of magnitude fainter than globular clusters with comparable half-light radii. At a heliocentric distance of 30 kpc, DES J0117–1725 is the second nearest of the new systems. DES J0117–1725 is detected predominantly by its main sequence stars and has one potential HB member. The lack of strong features in the color–magnitude distribution of stars associated with DES J0117–1725 leads to a large degeneracy between the distance, age, and metallicity of this system. If determined to be a dwarf galaxy, DES J0117–1725 would be the least luminous known galaxy; however, the current

classification of this object is ambiguous.

There are several gaps in the Y2Q1 coverage $\sim0°.1$ from DES J0117–1725; however, DES J0117–1725 is sufficiently compact that few member stars are expected in the region of missing coverage. These gaps are incorporated into the likelihood analysis and should have a minimal impact on the fit. The region around DES J0117–1725 was imaged in only a single r-band exposure; however, there are two to three overlapping exposures in each of the g- and i-bands. We have verified that the stellar overdensity is also apparent in the $g-i$ filter combination. Nonetheless, the properties of DES J0117–1725 should be interpreted with caution until additional imaging is acquired.

6.2. Satellite Detection Completeness

Many studies of the Milky Way satellite galaxy population require knowledge of the detection efficiency for satellites as a function of luminosity, heliocentric distance, physical size, and sky position in order to account for observational selection effects. To quantify our search sensitivity with the Y2Q1 data set, we follow the approach that Bechtol et al. (2015) applied to the DES Y1A1 coadd data. Briefly, we generated many realizations of satellite galaxies with different structural properties that are spread uniformly throughout the survey footprint, excluding regions of high stellar density near to the LMC. We then applied the map-based search algorithm to estimate the likelihood of a high-confidence detection. In the present implementation, the detection significance was evaluated as the Poisson probability of finding the "observed" number of stars within a circular region matched to the half-light radius of the simulated satellite given the effective local field density after the isochrone selection (see Section 3.1). Realizations that yield at least 10 detectable stars and produce a $>5.50\sigma$ overdensity within the half-light radius are considered "detected."

An essential input to the completeness calculation is the magnitude threshold for individual stars. For the searches described in Section 3, we used deeper magnitude thresholds (e.g., $g < 24$ mag) in order to maximize the discovery potential. A more conservative threshold, $g < 23$ mag, is selected to estimate the completeness in detecting new stellar systems

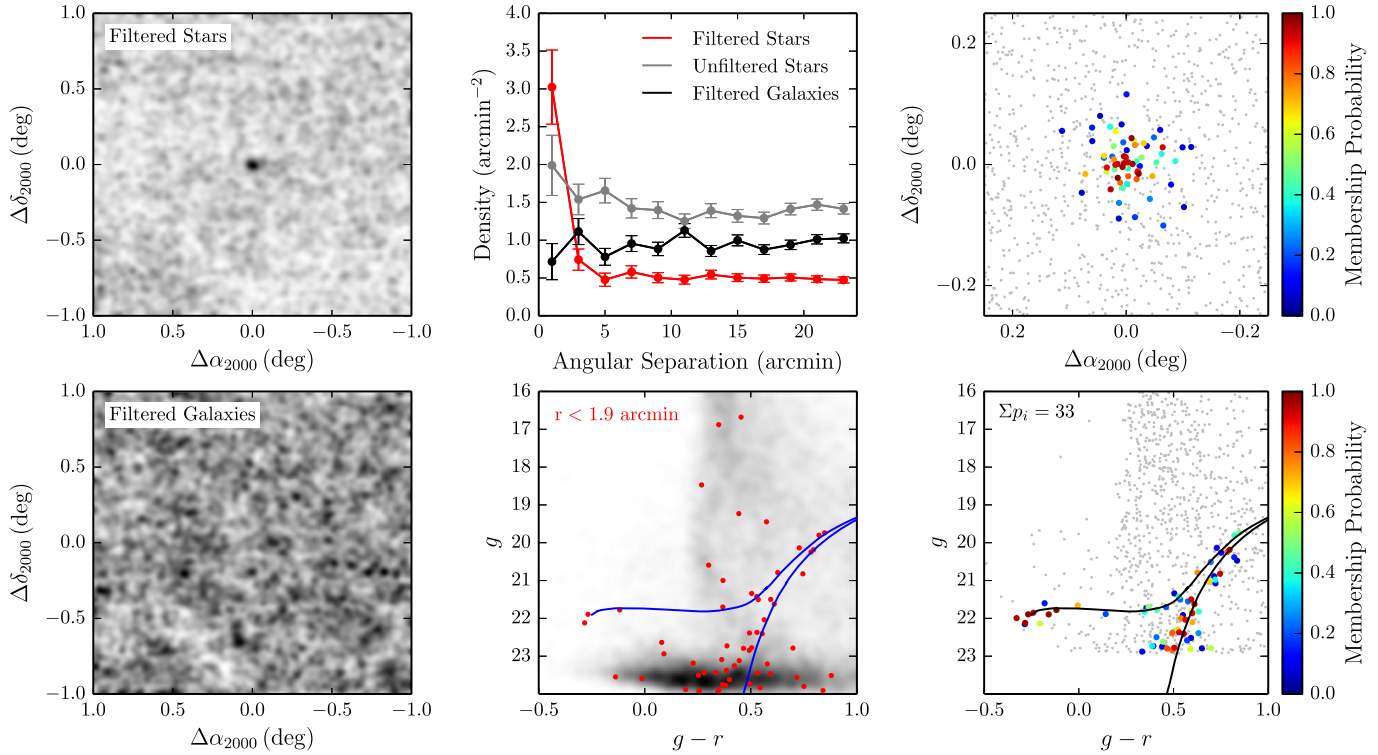DES J0531-2801 (Columba I); $(\alpha_{2000}, \delta_{2000}, m - M) = (82°86, -28°03, 21.30)$

Figure 9. Analogous to Figure 6 but for DES J0531–2801 (Columba I).

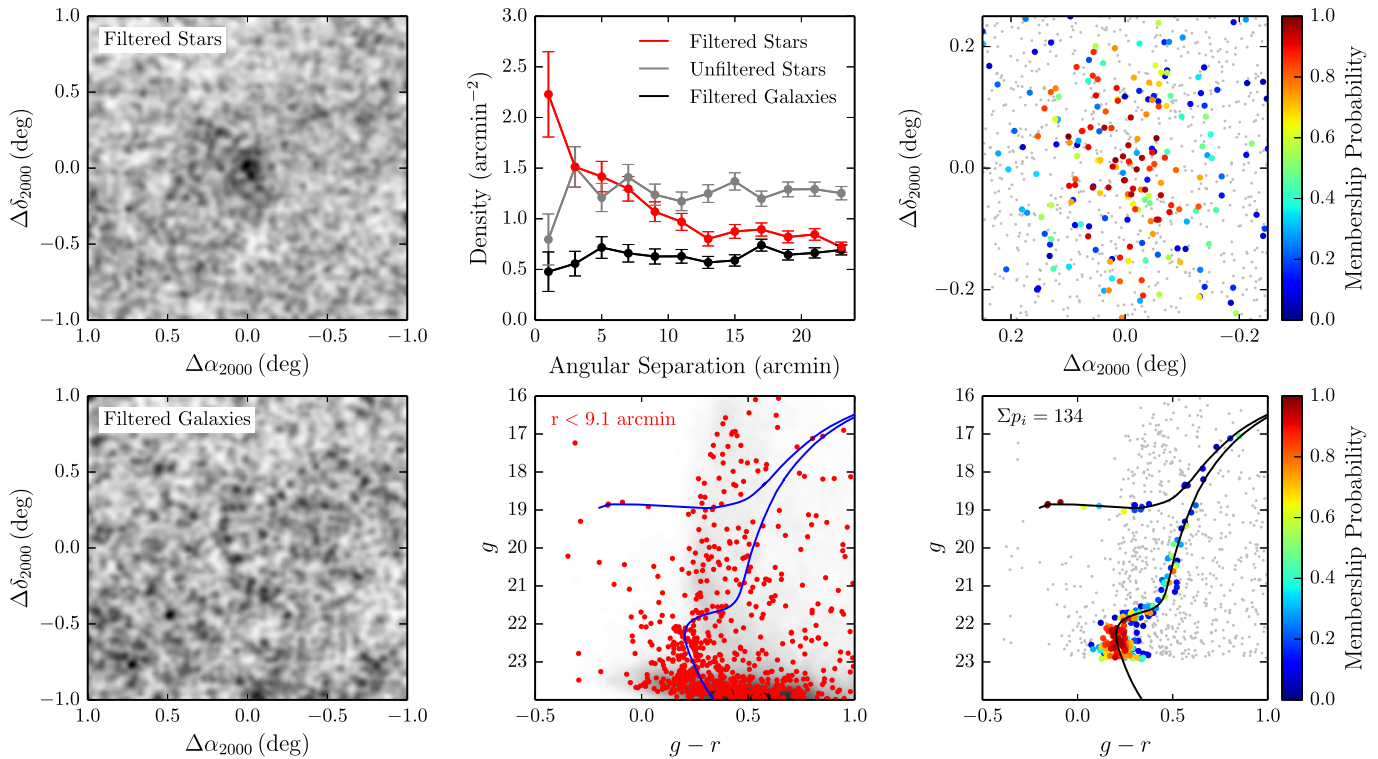DES J0002-6051 (Tucana IV); $(\alpha_{2000}, \delta_{2000}, m - M) = (0°73, -60°85, 18.41)$

Figure 10. Analogous to Figure 6 but for DES J0002–6051 (Tucana IV).

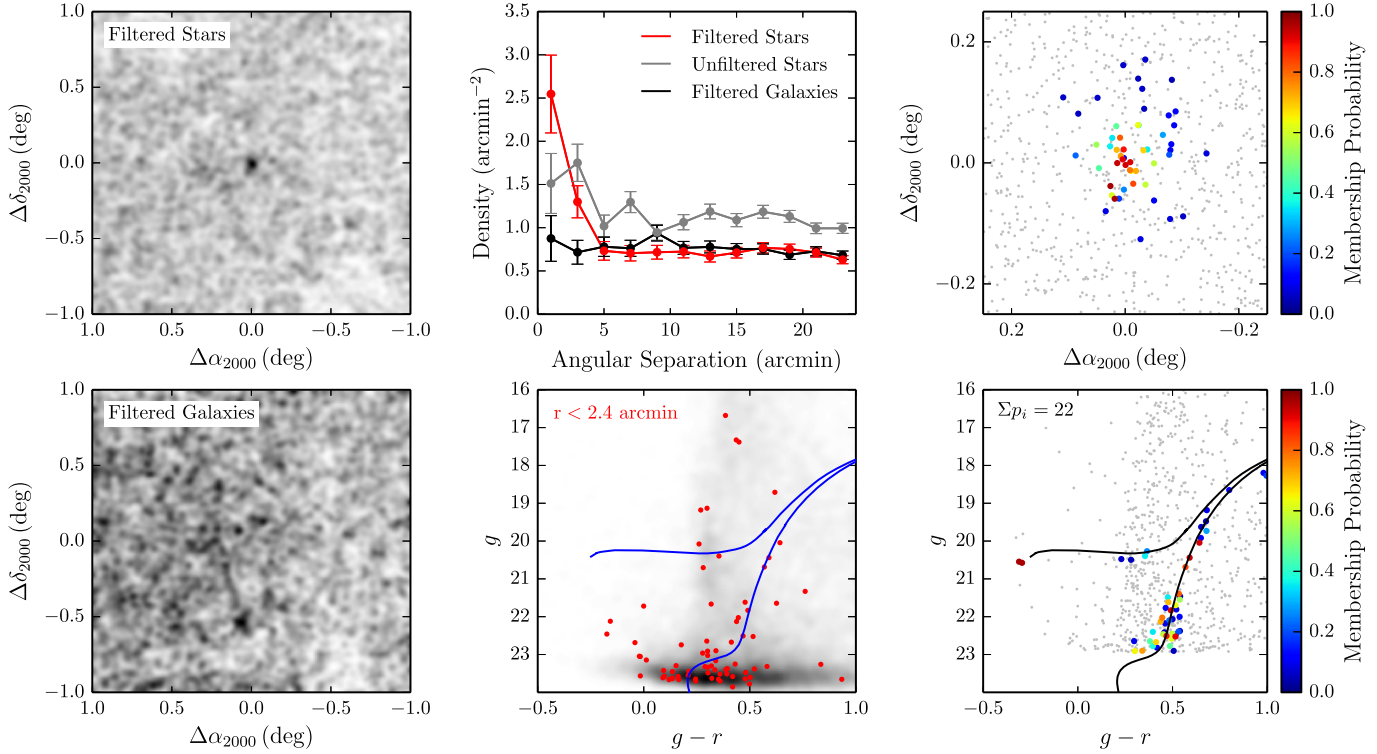DES J0345-6026 (Reticulum III); $(\alpha_{2000}, \delta_{2000}, m-M) = (56\overset{\circ}{.}36, -60\overset{\circ}{.}45, 19.81)$

Figure 11. Analogous to Figure 6 but for DES J0345–6026 (Reticulum III).

DES J2337-6316 (Tucana V); $(\alpha_{2000}, \delta_{2000}, m-M) = (354\overset{\circ}{.}35, -63\overset{\circ}{.}27, 18.71)$
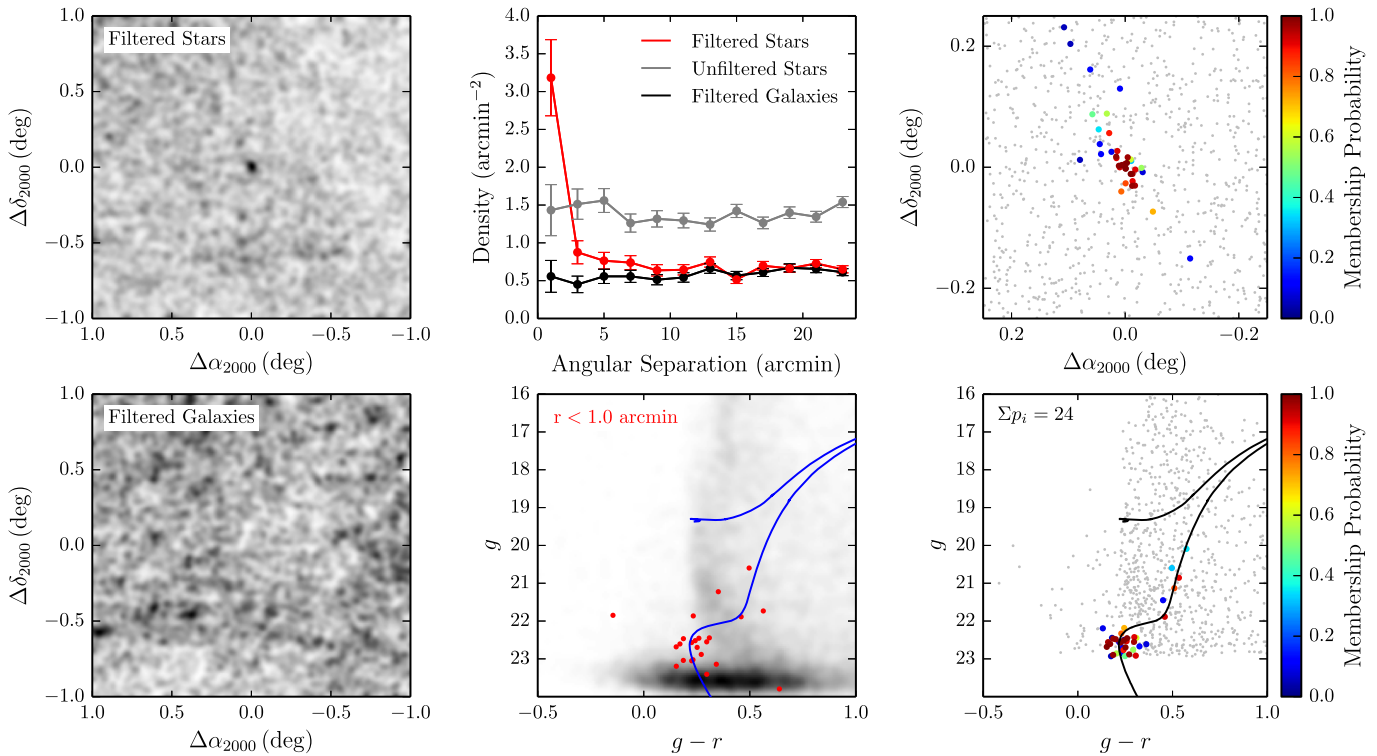
Figure 12. Analogous to Figure 6 but for DES J2337–6316 (Tucana V).

DES J2038-4609 (Indus II); $(\alpha_{2000}, \delta_{2000}, m - M) = (309\overset{\circ}{.}72, -46\overset{\circ}{.}16, 21.65)$
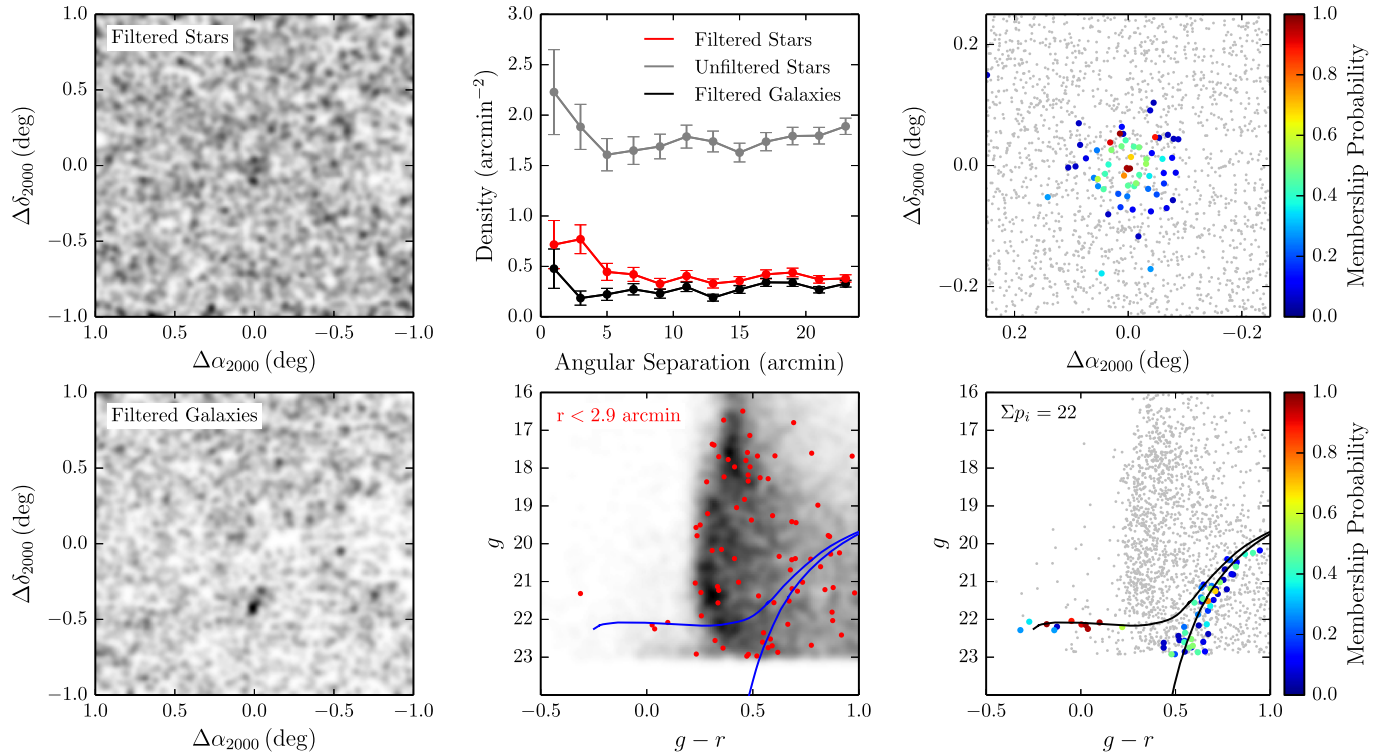
Figure 13. Analogous to Figure 6 but for DES J2038–4609 (Indus II). Note that the magnitude threshold for the smoothed counts maps and radial profiles has been raised to $g < 23$ mag due to non-uniform imaging depth in this region. DES J2038–4609 is detected primarily by a cluster of potential BHB members.

based on the following considerations. First, the Y2Q1 stellar sample is expected to be nearly complete for both Y1 and Y2 exposures at magnitudes $g \lesssim 23$ mag. Figure 3 shows that the measured stellar density in this magnitude range varies smoothly over the Y2Q1 footprint. At fainter magnitudes, discontinuities in the field density can occur in regions where exposures from Y1 and Y2 overlap (typically, more faint objects are detected in the Y2 exposures). Second, the field population with $g \gtrsim 23$ mag in high Galactic latitude regions is likely dominated by misclassified galaxies rather than halo stars, and therefore the assumption of isotropy on arcminute angular scales is compromised due to galaxy clustering. The adopted magnitude threshold matches that used in Bechtol et al. (2015), and in this case, the sensitivity estimates obtained in the prior work can be approximately scaled to the enlarged effective solid angle of the Y2Q1 data set, ~5000 deg^2.

In Table 4, we list the expected detection efficiencies for the DES ultra-faint galaxy candidates using magnitude thresholds of $g < 23$ mag and $g < 22$ mag, which roughly correspond to the stellar completeness limits of Y2Q1 and SDSS, respectively. For the brighter threshold, several of the DES candidates have substantially reduced detection probabilities.

We note that all of the faint stellar systems that were discovered in the Y1A1 data set are also significantly detected using the Y2Q1 data set, suggesting that our present search has sensitivity comparable to previous studies.

6.3. Total Number and Distribution of Milky Way Satellite Galaxies

The detection of 17 candidate ultra-faint galaxies in the first two years of DES data is consistent with the range of predictions based on the standard cosmological model (Tollerud et al. 2008; Hargis et al. 2014). These predictions model the spatial distribution of luminous satellites from the locations of dark matter subhalos in cosmological *N*-body simulations of Local Group analogs. Significant anisotropy in the distribution of satellites is expected (Tollerud et al. 2008; Hargis et al. 2014) and likely depends on the specific accretion history of the Milky Way (Deason et al. 2015).

The proximity of the DES footprint to the Magellanic Clouds is noteworthy when considering an anisotropic distribution of satellites. The possibility that some Milky Way satellites are or were associated with the Magellanic system has been discussed for some time (Lynden-Bell 1976; D'Onghia & Lake 2008; Nichols et al. 2011; Sales et al. 2011), and the recent DES results have renewed interest in this topic (Deason et al. 2015; Koposov et al. 2015a; Wheeler et al. 2015; Yozin & Bekki 2015). The existence of structures on mass scales ranging from galaxy clusters to ultra-faint satellite galaxies is a generic prediction of hierarchical galaxy formation in the cold dark matter paradigm. However, specific predictions for the number of observable satellites of the LMC and SMC depend on the still unknown efficiency of galaxy formation in low-mass subhalos. Identifying satellites of satellites within the Local Group would support the standard cosmological model, and may provide a new opportunity to test the impact of environment on the formation of the least luminous galaxies (Wetzel et al. 2015).

Based on a study of Milky Way–LMC analogs in *N*-body simulations, Deason et al. (2015) propose a method to evaluate the probability that a given satellite was at one time associated with the LMC based upon the present three-dimensional
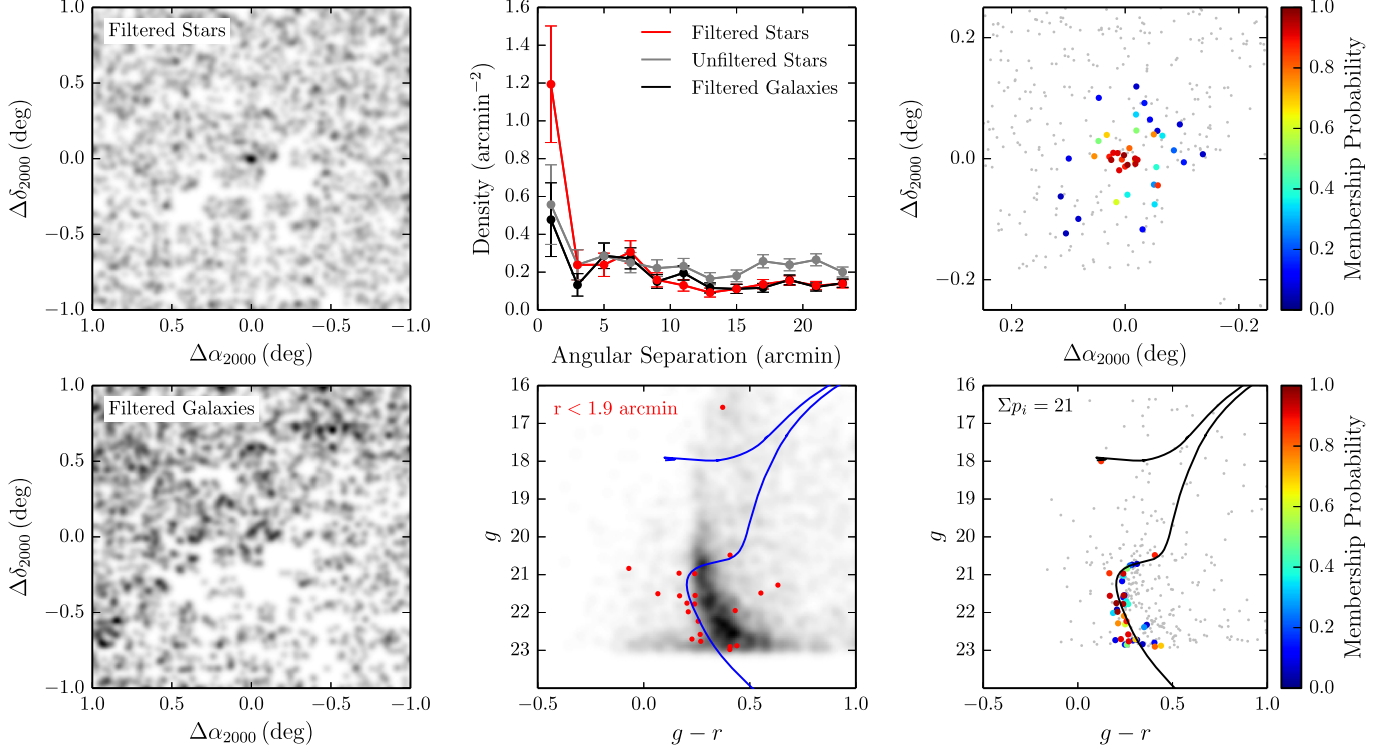
DES J0117–1725 (Cetus II); $(\alpha_{2000}, \delta_{2000}, m-M) = (19.47, -17.42, 17.38)$

Figure 14. Analogous to Figure 6 but for DES J0117–1725 (Cetus II). Note that the magnitude threshold for the smoothed counts maps and radial profiles has been raised to $g < 23$ mag due to incomplete coverage in this region.

Table 4
Expected Detection Efficiencies for Ultra-faint Galaxy Candidates

Name	M_V	Distance (kpc)	r_h (arcmin)	Efficiency ($g < 23$ mag)	Efficiency ($g < 22$ mag)
DES J2204–4626 (Gru II)	−3.9	53	6.0	1.00	0.39
DES J2356–5935 (Tuc III)	−2.4	25	6.0	1.00	0.94
DES J0531–2801 (Col I)	−4.5	182	1.9	0.95	0.86
DES J0002–6051 (Tuc IV)	−3.5	48	9.1	0.98	0.05
DES J0345–6026 (Ret III)	−3.3	92	2.4	0.33	0.05
DES J2337–6316 (Tuc V)	−1.6	55	1.0	0.94	0.01
DES J2038–4609 (Ind II)	−4.3	214	2.9	0.26	0.00
DES J0117–1725 (Cet II)	0.0	30	1.9	0.38	0.01
Ret II	−3.6	32	6.0	1.00	1.00
DES J0344.3–4331 (Eri II)	−7.4	330	1.8	1.00	1.00
DES J2251.2–5836 (Tuc II)	−3.9	58	7.2	1.00	0.07
Hor I	−3.5	87	2.4	0.66	0.14
DES J0443.8–5017 (Pic I)	−3.7	126	1.2	0.85	0.47
DES J0222.7–5217 (Eri III)	−2.4	95	0.4	0.41	0.04
DES J2339.9–5424 (Phe II)	−3.7	95	1.2	0.99	0.77
Gru I	−3.4	120	2.0	0.21	0.04
Hor II	−2.6	78	2.1	0.26	0.01

Note. Expected detection efficiencies are provided for two magnitude thresholds roughly corresponding to the stellar completeness depths of DES Y2Q1 ($g < 23$ mag) and SDSS ($g < 22$ mag). The detection efficiencies are estimated from multiple realizations of each candidate within the DES footprint using the best-fit luminosity M_V, heliocentric distance, and azimuthally averaged half-light radius r_h, which were then analyzed with the map-based detection algorithm described in Section 3.1. The average detection probability ratio between the two threshold choices is ~50%, implying that roughly half of the DES candidates would have been detected if they were located in the SDSS footprint.

separation between the two (Table 3). This prescription predicts that two to four of the Y2 DES candidates were associated with the LMC before infall, in addition to the two to four potentially associated satellites found in Y1 DES data. Deason et al. further suggest that a grouping of satellites near the LMC in

both physical separation and velocity would imply that the Magellanic system was recently accreted onto the Milky Way since members of this group would disperse within a few Gyr.

As a population, the new DES satellite galaxy candidates do appear to be unevenly distributed within the survey footprint;

15 are located at $\delta_{2000} < -40°$, close to the Magellanic Clouds (Figure 3). A Kolmogorov–Smirnov test, shown in Figure 15, significantly rejects the hypothesis of a uniform distribution ($p = 4.3 \times 10^{-4}$). One possible explanation for non-uniformity is that some of the new systems are satellites of the LMC or SMC. Below we introduce a simple model to test this hypothesis.

We began by modeling the probability distribution for detecting a satellite galaxy as a function of sky position. In this analysis, we excluded classical Milky Way satellites and considered only satellites that have similar characteristics to those discovered by DES (i.e., are detectable at the DES Y2Q1 depth). The underlying luminosity function and the completeness as a function of luminosity, heliocentric distance, and physical size were all simplified into a two-dimensional probability distribution.

We modeled this two-dimensional probability distribution with three components: (i) an isotropic distribution of satellites associated with the main halo of the Milky Way, (ii) a population of satellites spatially associated with the LMC halo, and (iii) a population of satellites spatially associated with the SMC halo. The first component was uniform on the sky, and the latter two components were spatially concentrated around the Magellanic Clouds. We assumed spherically symmetric three-dimensional distributions of satellites centered around each of the Magellanic Clouds having power-law radial profiles with slope $\alpha = -1$ and truncation radius $r_t = 35$ kpc. These distributions were then projected onto the sky to create two-dimensional predicted density maps.

Several underlying assumptions went into this simple model. First, we assumed that the Magellanic components were concentrated enough that variations in the completeness with respect to heliocentric distance would not substantially alter the projected density maps. Second, we assumed that the truncation radii of the LMC and SMC are the same, but later test the sensitivity of our results to this choice. Third, we assumed that smaller satellites of the Milky Way do not have their own associated satellites. We note that a power-law radial profile with slope $\alpha = -1$ can be viewed as a very extended Navarro–Frenk–White profile (Navarro et al. 1997). Since the DES footprint does not cover the central regions of the Magellanic Clouds, this shallow profile yields a conservative estimate on the fraction of satellites associated with the Magellanic system.

We performed an unbinned maximum-likelihood fit of our three-component model to the distribution of observed satellites. The parameters of the likelihood function are the total number of satellites and the relative normalizations of the three components. The likelihood is defined as the product of the probabilities to detect each observed satellite given its sky position. When presenting our results, we marginalized over the ratio of the LMC component to the SMC component. This ratio is not strongly constrained by our analysis; however, there is a slight preference for a larger SMC component.

The left panel of Figure 16 shows the constraints using the sky positions of the seventeen DES satellite galaxy candidates. We find that the DES data alone reject a uniform distribution of satellites at $>3\sigma$ confidence when compared to our best-fit model. This again implies that there is either a clear overdensity of satellites around the Magellanic Clouds or that the initial assumption of isotropy around the main halo is incorrect. In Figure 15, we show the distribution of declinations for our best-
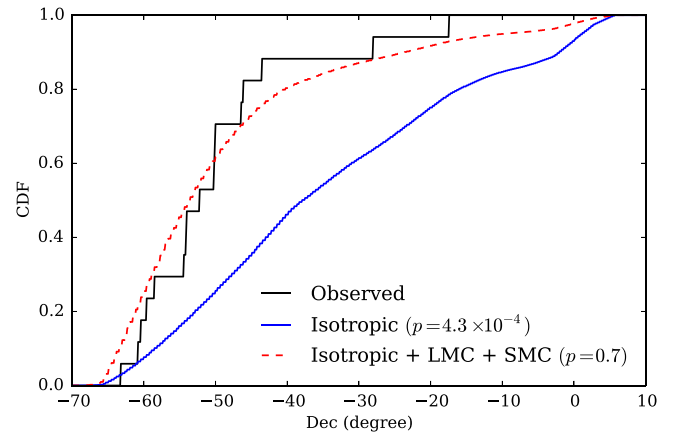
Figure 15. Cumulative distribution functions of declination values for the 17 observed satellites in the DES footprint (black), a uniform distribution given the shape of DES footprint (blue), and the best-fit model for a uniform distribution and Magellanic Cloud components (red dashed). See Section 6.3.

fit three-component model and find good agreement with the observations ($p = 0.7$).

We next tested the sensitivity of our result to the assumed distribution of satellites around the LMC and SMC. The central panel of Figure 16 shows the 1σ contours for three different values of $r_t = \{25, 35, 45 \text{ kpc}\}$, and two values of the slope, $\alpha = \{-1, -2\}$. Despite slight changes in the likelihood contours, in each case $>10\%$ of Milky Way satellites are likely to be spatially associated with the Magellanic Clouds.

We further examined the satellite population by simultaneously considering the 16 ultra-faint satellites observed in the SDSS DR10 footprint.[49] To fully combine DES and SDSS observations we would need to model the detection efficiency of SDSS relative to DES as a function of satellite distance, size, and luminosity. However, since the SDSS DR10 footprint only overlaps with the isotropic component in our model, we can again fold the complications of detection efficiency into a constant detection ratio. Our fiducial calculation assumes that 50% of the satellites discovered in DES would be detectable by SDSS, which agrees with the relative detection efficiency of the 17 DES satellites at the depth of SDSS (Table 4). The right panel of Figure 16 shows that the DES+SDSS constraints are in agreement with those from DES data alone, though the fraction of LMC and SMC satellites is more tightly constrained by including information from a large region widely separated from the Magellanic Clouds. The combined results imply that there are $\sim$100 satellites over the full sky that are detectable at DES Y2Q1 depth, and that 20%–30% of these might be associated with the Magellanic Clouds. Importantly, this prediction does not attempt to model the full population of Milky Way satellites beyond the DES Y2Q1 sensitivity and ignores the diminished detection efficiency close to the Galactic plane.

The Pan-STARRS team has recently identified three candidate Milky Way satellite galaxies in their 3π survey (Laevens et al. 2015a, 2015b). If this search is complete to the depth of SDSS over its full area, it is notable that so few candidates have been found. This observation alone could imply anisotropy without requiring the influence of the Magellanic Clouds. However, much of the Pan-STARRS area

---

[49] We include Pegasus III (Kim et al. 2015a) in the list of ultra-faint satellites from SDSS.
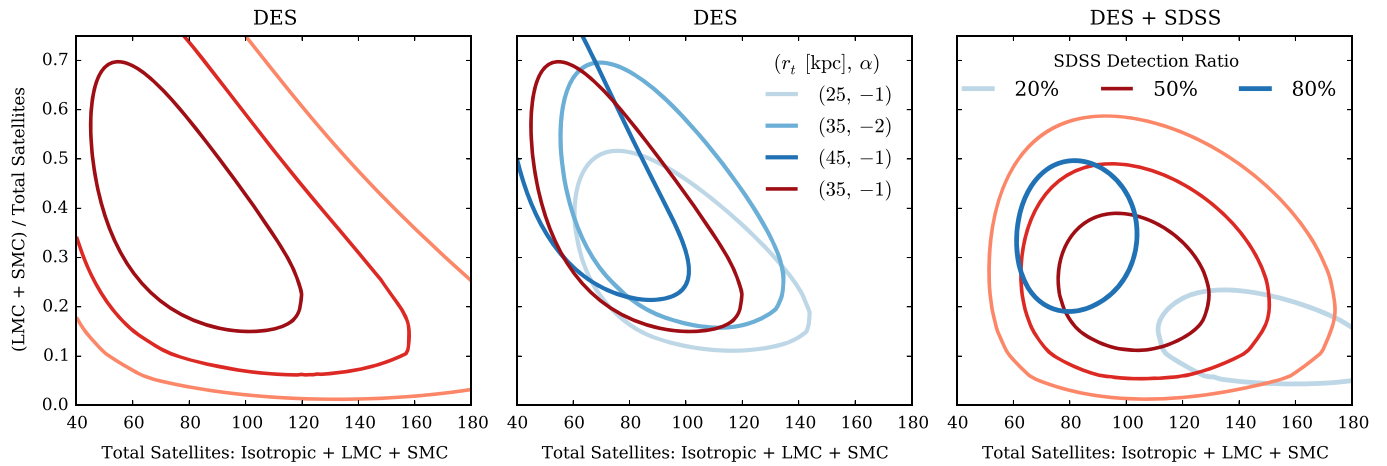
Figure 16. Maximum-likelihood fit to the spatial distribution of satellites for a model including isotropic, LMC, and SMC components (Section 6.3). The horizontal axis represents the total number of satellites detectable at DES Y2Q1 depth integrated over the entire sky (not including the classical dwarf galaxies and detection inefficiency near the Galactic plane). The vertical axis represents the fraction of these satellites associated with the Magellanic Clouds. Left: the 1σ, 2σ, and 3σ likelihood contours when considering only DES data. Center: 1σ contours for different values of the LMC and SMC truncation radius (r_t) and the slope of the radial profile (α). Right: contours of the likelihood function when SDSS observations are included. Red contours (1σ, 2σ, 3σ) assume that 50% of the satellites discovered in DES would have been detected if they were located in the SDSS footprint. This value matches the estimated detection efficiency from Table 4. We show the sensitivity of our results to the SDSS/DES detection ratio with the dark blue contour (80% detection ratio) and the light blue contour (20% detection ratio).

is located at low Galactic latitudes where the elevated foreground stellar density and interstellar extinction may present additional challenges. Under the assumption that Pan-STARRS covers the full sky with $\delta_{2000} > -30°$, $\sim 2000\,\mathrm{deg}^2$ overlap with DES Y2Q1. This area of the DES footprint includes two new candidates, one of which has a large enough surface brightness to likely have been detected at SDSS depth (DES J0531–2801, see Table 4). These two candidates are located in a region of the sky that would be observed at a relatively high airmass by Pan-STARRS and may suffer from decreased detection efficiency.

From this analysis, we conclude that the distribution of satellites around the Milky Way is unlikely to be isotropic, and that a plausible component of this anisotropy is a population of satellites associated with the Magellanic Clouds. However, several alternative explanations for anisotropy in the Milky Way satellite distribution exist. For example, Milky Way satellites could be preferentially located along a three-dimensional planar structure, as has been suggested by many authors, starting with Lynden-Bell (1976). This proposed planar structure encompasses the Magellanic Clouds and many of the classical and SDSS satellites. Pawlowski et al. (2015) suggest that the satellites discovered in Y1 DES data are also well aligned with this polar structure. We note that the Y2 discoveries presented here include several objects near the SMC and may reduce the fraction of objects in close proximity to the proposed plane. An additional possibility is that the satellites are associated with the orbit of the Magellanic System and are not isotropically distributed around the Magellanic Clouds themselves (Yozin & Bekki 2015). The DES footprint covers only a fraction of the region surrounding the Magellanic Clouds and additional sky coverage may yield more satellites with similar proximity to the Magellanic system and/or help to distinguish between these various scenarios. Measurements of the relative motions of the satellites and further theoretical work will also help clarify the physical relationships between these stellar systems.

7. CONCLUSIONS

We report the discovery of six new ultra-faint galaxy candidates in a combined data set from the first two years of DES covering $\sim 5000\,\mathrm{deg}^2$ of the south Galactic cap. Two additional candidates are identified in regions with incomplete or non-uniform coverage and should be viewed with lower confidence until additional imaging is obtained. The new satellites are faint ($M_V > -4.7$ mag) and span a wide range of physical sizes ($17\,\mathrm{pc} < r_{1/2} < 181\,\mathrm{pc}$) and heliocentric distances ($25\,\mathrm{kpc} < D_\odot < 214\,\mathrm{kpc}$). All are low surface brightness systems similar to the known ultra-faint satellite galaxies of the Milky Way, and most possess physical sizes that are large enough ($>40\,\mathrm{pc}$) to be provisionally classified as galaxies. Spectroscopic observations are needed to better understand and unambiguously classify the new stellar systems. A total of 17 confirmed and candidate ultra-faint galaxies have been found in the first two years of DES. Roughly half of the DES systems are sufficiently distant and/or faint to have eluded detection at survey depths comparable to SDSS.

The DES satellites are concentrated in the southern half of the survey footprint in proximity to the Magellanic Clouds. In addition, we find three satellites clustered in a Tucana group, each of which is within $<10\,\mathrm{kpc}$ of the group centroid. We find that the DES data alone exclude ($p < 10^{-3}$) an isotropic distribution of satellites within the Milky Way halo, and that the observed distribution can be well, although not uniquely, explained by a model in which several of the observed DES satellites are associated with the Magellanic system. Under the assumption that the total satellite population can be modeled by isotropic distributions around the Milky Way, LMC, and SMC, we estimate that a total of ~ 100 ultra-faint satellites with comparable physical characteristics to those detected by DES might exist over the full sky, with 20%–30% of these systems being spatially associated with the Magellanic Clouds.

Milky Way satellite galaxies are considered a unique population for studying the particle nature of dark matter due to their proximity, characteristically large mass-to-light ratios,

and lack of intrinsic astrophysical backgrounds. Although the dark matter content of the new stellar systems has not yet been spectroscopically confirmed, the possibility that some are dark matter dominated galaxies makes them interesting targets for indirect dark matter searches via gamma rays. No gamma-ray sources from the third *Fermi*-LAT source catalog (3FGL; Acero et al. 2015) are located within $0°\!.5$ of any of the new candidates. A follow-up gamma-ray analysis of these ultra-faint galaxy candidates will be presented separately.

Future seasons of DES will not significantly increase the DES sky coverage. However, there will be considerable gains in depth from the expected 10 tilings per filter relative to the two to four in the Y2Q1 data set. This increased depth will expand the effective volume of the survey. In addition, we expect the survey uniformity to improve with the coming seasons, resulting in a cleaner list of seeds with fewer false positives. Star-galaxy separation may become a limiting factor at the future depth of DES, motivating the development of improved classification algorithms (e.g., Fadely et al. 2012; Soumagnac et al. 2015), as well as alternative search strategies, involving, for instance, the time domain (Baker & Willman 2015) or stellar velocities (Antoja et al. 2015). While it is likely that the most conspicuous Milky Way satellites in the DES footprint have been found, the most exciting phase of Milky Way science with DES is likely still to come. The wide area and growing sensitivity of DES will enable the discovery of dwarf galaxies that are fainter, farther, and have lower surface brightness.

REFERENCES

Abbott, T., Aldering, G., Annis, J., et al. 2005, arXiv:astro-ph/0510346
Acero, F., Ackermann, M., Ajello, M., et al. 2015, ApJS, 218, 23
Ackermann, M., et al. 2015, PRL, in press (arXiv:1503.02641)
Adén, D., Feltzing, S., Koch, A., et al. 2009, A&A, 506, 1147
Antoja, T., Mateu, C., Aguilar, L., et al. 2015, MNRAS, 453, 541
Astropy Collaboration, Robitaille, T. P., Tollerud, E. J., et al. 2013, A&A, 558, A33
Baker, M., & Willman, B. 2015, AJ, in press (arXiv:1507.00734)
Balbinot, E., Santiago, B. X., da Costa, L. N., Makler, M., & Maia, M. A. G. 2011, MNRAS, 416, 393
Balbinot, E., Santiago, B. X., da Costa, L., et al. 2013, ApJ, 767, 101
Bechtol, K., Drlica-Wagner, A., Balbinot, E., et al. 2015, ApJ, 807, 50
Belokurov, V., Irwin, M. J., Koposov, S. E., et al. 2014, MNRAS, 441, 2124
Belokurov, V., Walker, M. G., Evans, N. W., et al. 2008, ApJL, 686, L83
Belokurov, V., Walker, M. G., Evans, N. W., et al. 2009, MNRAS, 397, 1748
Belokurov, V., Walker, M. G., Evans, N. W., et al. 2010, ApJL, 712, L103
Belokurov, V., Zucker, D. B., Evans, N. W., et al. 2006, ApJL, 647, L111
Belokurov, V., Zucker, D. B., Evans, N. W., et al. 2007, ApJ, 654, 897
Benson, A. J., Frenk, C. S., Lacey, C. G., Baugh, C. M., & Cole, S. 2002, MNRAS, 333, 177
Bertin, E. 2006, in ASP Conf. Ser. 351, Astronomical Data Analysis Software and Systems XV, ed. C. Gabriel et al. (San Francisco, CA: ASP), 112
Bertin, E. 2011, in ASP Conf. Ser. 442, Astronomical Data Analysis Software and Systems XX, ed. I. N. Evans et al. (San Francisco, CA: ASP), 435
Bertin, E., & Arnouts, S. 1996, A&AS, 117, 393
Bressan, A., Marigo, P., Girardi, L., et al. 2012, MNRAS, 427, 127
Bullock, J. S., Kravtsov, A. V., & Weinberg, D. H. 2000, ApJ, 539, 517
Bullock, J. S., Kravtsov, A. V., & Weinberg, D. H. 2001, ApJ, 548, 33
Carlin, J. L., Grillmair, C. J., Muñoz, R. R., Nidever, D. L., & Majewski, S. R. 2009, ApJL, 702, L9
Chabrier, G. 2001, ApJ, 554, 1274
Chang, C., Busha, M. T., Wechsler, R. H., et al. 2015, ApJ, 801, 73
Corwin, H. G. 2004, yCat, 7239, 0
Coupon, J., Kilbinger, M., McCracken, H. J., et al. 2012, A&A, 542, A5
de Grijs, R., & Bono, G. 2015, AJ, 149, 179
de Grijs, R., Wicker, J. E., & Bono, G. 2014, AJ, 147, 122
Deason, A. J., Wetzel, A. R., Garrison-Kimmel, S., & Belokurov, V. 2015, MNRAS, 453, 3568
Desai, S., Armstrong, R., Mohr, J. J., et al. 2012, ApJ, 757, 83
Dickey, J. M. 1971, Ann. Math. Statist., 42, 204
D'Onghia, E., & Lake, G. 2008, ApJL, 686, L61
Dotter, A., Chaboyer, B., Jevremović, D., et al. 2008, ApJS, 178, 89
Drlica-Wagner, A., Albert, A., Bechtol, K., et al. 2015, ApJL, 809, L4
Erben, T., Hildebrandt, H., Miller, L., et al. 2013, MNRAS, 433, 2545
Fadely, R., Hogg, D. W., & Willman, B. 2012, ApJ, 760, 15

Fadely, R., Willman, B., Geha, M., et al. 2011, AJ, 142, 88
Flaugher, B., Diehl, H. T., Honscheid, K., et al. 2015, AJ, submitted (arXiv:1504.02900)
Foreman-Mackey, D., Hogg, D. W., Lang, D., & Goodman, J. 2013, PASP, 125, 306
Geha, M., Willman, B., Simon, J. D., et al. 2009, ApJ, 692, 1464
Geringer-Sameth, A., Koushiappas, S. M., & Walker, M. G. 2015a, PhRvD, 91, 083535
Geringer-Sameth, A., Walker, M. G., Koushiappas, S. M., et al. 2015b, PhRvL, 115, 081101
Gilbank, D. G., Gladders, M. D., Yee, H. K. C., & Hsieh, B. C. 2011, AJ, 141, 94
Górski, K. M., Hivon, E., Banday, A. J., et al. 2005, ApJ, 622, 759
Grillmair, C. J. 2006, ApJL, 645, L37
Grillmair, C. J. 2009, ApJ, 693, 1118
Hargis, J. R., Willman, B., & Peter, A. H. G. 2014, ApJL, 795, L13
Harris, W. E. 1996, AJ, 112, 1487
Heymans, C., van Waerbeke, L., Miller, L., et al. 2012, MNRAS, 427, 146
High, F. W., Stubbs, C. W., Rest, A., Stalder, B., & Challis, P. 2009, AJ, 138, 110
Hooper, D., & Linden, T. 2015, arXiv:1503.06209
Irwin, M. J., Belokurov, V., Evans, N. W., et al. 2007, ApJL, 656, L13
Ivezić, Ž., Lupton, R. H., Schlegel, D., et al. 2004, AN, 325, 583
Kelly, P. L., von der Linden, A., Applegate, D. E., et al. 2014, MNRAS, 439, 28
Kharchenko, N. V., Piskunov, A. E., Schilbach, E., Röser, S., & Scholz, R.-D. 2013, A&A, 558, A53
Kim, D., & Jerjen, H. 2015a, ApJ, 799, 73
Kim, D., & Jerjen, H. 2015b, ApJL, 808, L39
Kim, D., Jerjen, H., Mackey, D., da Costa, G. S., & Milone, A. P. 2015a, ApJL, 804, L44
Kim, D., Jerjen, H., Milone, A. P., Mackey, D., & da Costa, G. S. 2015b, ApJ, 803, 63
Kirby, E. N., Boylan-Kolchin, M., Cohen, J. G., et al. 2013, ApJ, 770, 16
Kirby, E. N., Simon, J. D., & Cohen, J. G. 2015, ApJ, 810, 56
Kirby, E. N., Simon, J. D., Geha, M., Guhathakurta, P., & Frebel, A. 2008, ApJL, 685, L43
Kleyna, J. T., Wilkinson, M. I., Evans, N. W., & Gilmore, G. 2005, ApJL, 630, L141
Koch, A., Wilkinson, M. I., Kleyna, J. T., et al. 2009, ApJ, 690, 453
Koposov, S., Belokurov, V., Evans, N. W., et al. 2008, ApJ, 686, 279
Koposov, S., de Jong, J. T. A., Belokurov, V., et al. 2007, ApJ, 669, 337
Koposov, S. E., Belokurov, V., Torrealba, G., & Evans, N. W. 2015a, ApJ, 805, 130
Koposov, S. E., Casey, A. R., Belokurov, V., et al. 2015b, ApJ, in press (arXiv:1504.07916)
Koposov, S. E., Gilmore, G., Walker, M. G., et al. 2011, ApJ, 736, 146
Laevens, B. P. M., Martin, N. F., Bernard, E. J., et al. 2015a, ApJ, submitted (arXiv:1507.07564)
Laevens, B. P. M., Martin, N. F., Ibata, R. A., et al. 2015b, ApJL, 802, L18
Laevens, B. P. M., Martin, N. F., Sesar, B., et al. 2014, ApJL, 786, L3
Luque, E., Queiroz, A., Santiago, B., et al. 2015, MNRAS, in press (arXiv:1508.02381)
Lynden-Bell, D. 1976, MNRAS, 174, 695
MacDonald, E. C., Allen, P., Dalton, G., et al. 2004, MNRAS, 352, 1255
Martin, N. F., de Jong, J. T. A., & Rix, H.-W. 2008, ApJ, 684, 1075
Martin, N. F., Ibata, R. A., Chapman, S. C., Irwin, M., & Lewis, G. F. 2007, MNRAS, 380, 281

Martin, N. F., Nidever, D. L., Besla, G., et al. 2015, ApJL, 804, L5
McClure-Griffiths, N. M., Pisano, D. J., Calabretta, M. R., et al. 2009, ApJS, 181, 398
McConnachie, A. W. 2012, AJ, 144, 4
Mohr, J. J., Armstrong, R., Bertin, E., et al. 2012, Proc. SPIE, 8451, 84510D
Muñoz, R. R., Carlin, J. L., Frinchaboy, P. M., et al. 2006, ApJL, 650, L51
Muñoz, R. R., Geha, M., Côté, P., et al. 2012, ApJL, 753, L15
Muñoz, R. R., Majewski, S. R., & Johnston, K. V. 2008, ApJ, 679, 346
Navarro, J. F., Frenk, C. S., & White, S. D. M. 1997, ApJ, 490, 493
Neilsen, E., Bernstein, G., Gruendl, R., & Kent, S. 2015, Limiting Magnitude, τ, $T_{\rm eff}$, and Image Quality in DES Year 1, Tech. Rep. FERMILAB-TM-2610-AE-CD (Batavia, IL: Fermi National Accelerator Laboratory)
Nichols, M., Colless, J., Colless, M., & Bland-Hawthorn, J. 2011, ApJ, 742, 110
Nilson, P. 1973, Uppsala General Catalogue of Galaxies (Uppsala: Royal Society of Sciences in Uppsala)
Oh, K. S., Lin, D. N. C., & Aarseth, S. J. 1995, ApJ, 442, 142
Ortolani, S., Bica, E., & Barbuy, B. 2013, MNRAS, 433, 1966
Paust, N., Wilson, D., & van Belle, G. 2014, AJ, 148, 19
Pawlowski, M. S., McGaugh, S. S., & Jerjen, H. 2015, MNRAS, 453, 1047
Peñarrubia, J., Navarro, J. F., & McConnachie, A. W. 2008, ApJ, 673, 226
Putman, M. E., Staveley-Smith, L., Freeman, K. C., Gibson, B. K., & Barnes, D. G. 2003, ApJ, 586, 170
Rykoff, E. S., Rozo, E., Busha, M. T., et al. 2014, ApJ, 785, 104
Sakamoto, T., & Hasegawa, T. 2006, ApJL, 653, L29
Sales, L. V., Navarro, J. F., Cooper, A. P., et al. 2011, MNRAS, 418, 648
Schlafly, E. F., & Finkbeiner, D. P. 2011, ApJ, 737, 103
Schlegel, D. J., Finkbeiner, D. P., & Davis, M. 1998, ApJ, 500, 525
Sevilla, I., Armstrong, R., Bertin, E., et al. 2011, in Proc. DPF-2011 Conf., Providence, RI, 8–13 August 2011
Simon, J., Drlica-Wagner, A., Li, T. S., et al. 2015, ApJ, 808, 95
Simon, J. D., & Geha, M. 2007, ApJ, 670, 313
Simon, J. D., Geha, M., Minor, Q. E., et al. 2011, ApJ, 733, 46
Soumagnac, M. T., Abdalla, F. B., Lahav, O., et al. 2015, MNRAS, 450, 666
Tollerud, E. J., Bullock, J. S., Strigari, L. E., & Willman, B. 2008, ApJ, 688, 277
Trotta, R. 2007, MNRAS, 378, 72
van den Bergh, S. 2008, AJ, 135, 1731
Walker, M. G., Belokurov, V., Evans, N. W., et al. 2009, ApJL, 694, L144
Walker, M. G., Mateo, M., Olszewski, E. W., et al. 2015, ApJ, 808, 108
Walsh, S. M., Jerjen, H., & Willman, B. 2007, ApJL, 662, L83
Walsh, S. M., Willman, B., & Jerjen, H. 2009, AJ, 137, 450
Westmeier, T., Staveley-Smith, L., Calabretta, M., et al. 2015, MNRAS, 453, 338
Wetzel, A. R., Deason, A. J., & Garrison-Kimmel, S. 2015, ApJ, 807, 49
Wheeler, C., Oñorbe, J., Bullock, J. S., et al. 2015, MNRAS, 453, 1305
Willman, B. 2010, AdAst, 2010, 21
Willman, B., Blanton, M. R., West, A. A., et al. 2005a, AJ, 129, 2692
Willman, B., Dalcanton, J. J., Martinez-Delgado, D., et al. 2005b, ApJL, 626, L85
Willman, B., Geha, M., Strader, J., et al. 2011, AJ, 142, 128
Willman, B., & Strader, J. 2012, AJ, 144, 76
York, D. G., Adelman, J., Anderson, J. E., Jr., et al. 2000, AJ, 120, 1579
Yozin, C., & Bekki, K. 2015, MNRAS, 453, 2302
Zacharias, N., Finch, C. T., Girard, T. M., et al. 2013, AJ, 145, 44
Zucker, D. B., Belokurov, V., Evans, N. W., et al. 2006a, ApJL, 650, L41
Zucker, D. B., Belokurov, V., Evans, N. W., et al. 2006b, ApJL, 643, L103